A stable discretization of the lattice Boltzmann equation for simulation of incompressible two-phase flows at high density ratio

Taehun Lee, Ching-Long Lin *

*Department of Mechanical and Industrial Engineering, IIHR – Hydroscience & Engineering, The University of Iowa,
Iowa City, IA 52242-1527, USA*

Abstract

A stable discretization of the lattice Boltzmann equation (LBE) for non-ideal gases is presented for simulation of incompressible two-phase flows having high density and viscosity ratios. The stiffness of the discretized forcing terms in LBE for non-ideal gases is known to trigger severe numerical instability and restrict practical application of the LBE method. Use of a proper pressure updating scheme is also crucial to the stability of the LBE method because of non-negligible pressure variation across the phase interface. To deal with these issues, we propose a stable discretization scheme, which assumes the low Mach number approximation, and utilizes the stress and potential forms of the surface tension force, the incompressible transformation, and the consistent discretization of the intermolecular forcing terms. The proposed stable discretization scheme is applied to simulate 1-D advection equation with a source term, a stationary droplet, droplet oscillation and droplet splashing and deposition on a thin film at a density ratio of 1000 with varying Reynolds numbers. The numerical solutions of stationary and oscillatory droplets agree well with analytic solutions including the Laplace's law. The time history of the spread factor of the liquid sheet emitted after the droplet impact also follows the known spreading power law.
© 2004 Elsevier Inc. All rights reserved.

Keywords: Lattice Boltzmann method; High density ratio; Droplet splashing

1. Introduction

Any phase interface boundary is mesoscopic by nature [1]. The gradients of material properties in the normal direction of the interface are steep, approaching a molecular scale, which makes it necessary to

* Corresponding author. Tel.: +1 319 335 5673; fax: +1 319 335 5669.
  E-mail address: ching-long-lin@uiowa.edu (C.-L. Lin).

consider microscopic factors that effect larger scales. In this regard, the lattice Boltzmann equation (LBE) is based on microscopic models and mesoscopic kinetic equations [2]. Even though major focus of the LBE method has been on averaged macroscopic behavior, its kinetic nature can provide many of the advantages of molecular dynamics, which are especially useful for simulation of phase interfaces of non-ideal gases or binary fluids [3–12] and near wall treatment at micro-fluid level [13–16]. Most of these two-phase LBE methods can be considered as diffuse interface methods [17] in that the phase interface is spread on grid points and the surface tension is transformed into a volumetric force. Generally, diffuse interface methods have some theoretical and numerical advantages over sharp interface methods. Usually, computations are much easier for three-dimensional (3-D) flows in which topological change of the interfaces is complicated. Diffuse interface methods are particularly useful for phase change problems [18,19], since the speed of displacement of the interface must be explicitly computed in sharp interface methods. Furthermore, diffuse interface methods are especially appropriate for some problems that are currently tough for sharp interface methods such as contact line dynamics and coalescence of droplets. As a diffuse interface method, the LBE method naturally shares all of these characteristics.

Recently, He et al. [20] proposed a novel LBE formulation for non-ideal gases based on the continuous discrete Boltzmann equation (DBE) using a single-relaxation-time approximation [21]. Phase separation is induced by mechanical instability in the supernodal curve of the phase diagram. The intermolecular interactions for simulation of non-ideal gas effects are derived from the Enskog extension of the Boltzmann equation. Naturally, implementation of the thermodynamical concept is more flexible than some of the previous LBE models such as the Shan and Chen (SC) model [4,5,8]. An analysis of the SC model that incorporates intermolecular forces into ideal gas LBE methods was clearly performed in the framework of the proposed formulation. He et al. found that the anisotropy reported in the SC model is a consequence of inappropriate intermolecular interaction. Also, Galilean invariance plaguing the free-energy-based model of Swift et al. [6,7,22] was effectively removed from their formulation.

However, criticisms against the He et al.'s original model have been raised, which are mostly regarding numerical instability [19,23], especially for two fluids having moderate to high density ratios. To stabilize otherwise unstable original formulation, He and coworkers [9–12] proposed a modified LBE formulation. Using the modified formulation, they simulated single-mode and multiple-mode Rayleigh–Taylor instabilities in 2-D and 3-D, reporting excellent results. Later, they included the surface tension effect into the model and studied the effects of the surface tension force on two-phase Kelvin–Helmholtz instability. The modification proposed by He et al. [9] is based upon the transformation of the particle distribution function for mass and momentum into that for hydrodynamic pressure and momentum. As a direct consequence of the transformation, the compressible Navier–Stokes equations become the nearly-incompressible Navier–Stokes equations [19]. He et al. argued that the enhanced stability of the modified formulation was due to reduction of discretization error of the forcing term, i.e., the leading order of the intermolecular forcing terms was reduced from O(1) to O(**u**). Another particle distribution function was introduced for order parameter, specifically, density in the case of non-ideal gases. Maximum density ratio in their simulation of the Rayleigh–Taylor instability was reported up to 20, which is quite impressive considering that most of the previous LBE simulations had been performed at density ratios of around 2.

While reduction of discretization error of the intermolecular forcing terms is one crucial factor that effects numerical stability of the LBE method, pressure updating scheme is an equally important factor. The pressure in the He et al.'s original LBE formulation [20] is updated using the non-ideal gas equation of state (EOS). In contrast, the pressure in the modified LBE formulation [9] is rather a hydrodynamic pressure whose role is simply to satisfy the approximate divergence-free condition. The profile of the hydrodynamic pressure in the phase interface is generally smoother than that of the thermodynamic pressure, although the smoothness of the hydrodynamic pressure is strongly affected by the surface tension force. If the Mach number (*Ma*) is small, further simplification is possible. In this case, the hydrodynamic pressure becomes

several orders of magnitude smaller than the thermodynamic pressure, and the higher-order terms related to the hydrodynamic pressure can be neglected [24,25].

In fact, there have been increasing efforts to improve the stability of two-phase LBE models at high density ratio. For instance, Teng et al. [26] discretized the DBE of He et al. [20] using the total variation diminishing (TVD) with artificial dissipation scheme. The collision term and the intermolecular forcing terms were treated as explicit source terms for the advection equation, and the advection equation is discretized in time with the second-order Runge–Kutta scheme [27]. With the aid of the TVD discretization they could stabilize otherwise unstable LBE formulation and was able to simulate dam breaking case at a density ratio of 1000, although quantitative comparison with existing experimental or numerical results was not provided. However, it is noteworthy that explicit treatment of both the collision and the intermolecular forcing terms with the second-order Runge–Kutta time-marching method can severely restrict the range of the relaxation time and the Reynolds number (*Re*) [28]. TVD schemes usually take much more computing time and memory than the simple perfect-shift in the LBE method. In addition, TVD schemes inevitably reduce accuracy in the presence of non-smooth gradient by adding numerical dissipation, which necessitates study of the effect of additional dissipation on the accuracy of the LBE solutions. More recently, Inamuro et al. [29,30] proposed an interesting approach based on Swift et al.'s free-energy-based model. The model requires two particle distribution functions: one for the order parameter which represents the phase of the fluids and the other for the predicted velocity of the two fluids without a pressure gradient. The model is then supplemented by the relation between the velocity and the pressure correction which is determined by solving an approximate pressure Poisson equation. Their method was applied to a single rising bubble in liquid and many bubbles rising in a square duct with a fixed relaxation time of $\tau = 1$. Nevertheless, solving pressure Poisson equation not only undermines the simplicity of the LBE method but increases computational loads. The difference between the projected pressure obtained by solving the approximate pressure Poisson equation and the pressure computed from EOS remains unclear as well.

The stable discretization proposed in the present study is a collection of consistent discretization strategies. It comprises the low Mach number approximation, the use of stress and potential forms of the surface tension force, the incompressible transformation, and the consistent discretization of the intermolecular forcing terms. The benchmark cases for the stable discretization include 1-D advection equation with a source term, stationary and oscillatory droplets, and droplet splashing on a thin liquid film at a density ratio of 1000 with viscosity ratio varying from 40 to 1000. The corresponding relaxation time τ ranges from 0.006 to 0.15. The proposed fully implicit formulation of LBE does not require the iteration procedure as proposed by Sankaranarayanan et al. [31] and the resulting LBE method is able to simulate flows at large density and viscosity ratios without resort to either the TVD discretization or solving the pressure Poisson equation.

The paper is organized as follows. In Section 2, the two-distribution DBEs for non-ideal gas are presented. The role of pressure and surface tension in accuracy and stability of the DBEs is examined. In Section 3, the two-distribution DBEs are discretized to yield LBEs for incompressible flows and the consistent discretization schemes for the intermolecular forcing terms are discussed. Various benchmark cases such as solution of 1-D advection equation with a source term, stationary and oscillatory droplets, and droplet splashing on a thin liquid film are presented in Section 4. Concluding remarks are given in Section 5.

2. Mathematical model

2.1. Review

The Boltzmann equation for isothermal non-ideal gases with the BGK collision model can be written as [20]

$$\frac{\partial f}{\partial t} + \xi_i \frac{\partial f}{\partial x_i} + F_i \frac{\partial f}{\partial \xi_i} = -\frac{f - f^{\text{eq}}}{\lambda}, \tag{1}$$

where $f \equiv f(x_i, \xi_i, t)$ is the single-particle distribution function in the phase space (x_i, ξ_i), ξ_i is the microscopic velocity, F_i is an external body force, λ is the relaxation time due to collision, and f^{eq} is the Maxwell–Boltzmann distribution function. Since the derivative $\partial_{\xi_i} f$ cannot be calculated directly, He et al. [20] took the equilibrium distribution function f^{eq} as the leading part of the distribution function and approximated the derivative as

$$\frac{\partial f}{\partial \xi_i} \approx \frac{\partial f^{\text{eq}}}{\partial \xi_i} = -\frac{\xi_i - u_i}{c_s^2} f^{\text{eq}}, \tag{2}$$

in which c_s is the lattice speed of sound.

With this approximation, discretization of the microscopic velocity field ξ_i on unit lattice yields the DBE with discretized microscopic velocity e_α:

$$\frac{Df_\alpha}{Dt} = \frac{\partial f_\alpha}{\partial t} + e_{\alpha i} \frac{\partial f_\alpha}{\partial x_i} = -\frac{1}{\lambda}\left(f_\alpha - f_\alpha^{\text{eq}}\right) + \frac{(e_{\alpha i} - u_i)F_i}{\rho c_s^2} f_\alpha^{\text{eq}}, \tag{3}$$

where f_α is the particle distribution function in the α direction of a lattice model, $e_{\alpha i}$ is the i-component of the α-direction microscopic velocity, and ρ is the density normalized to the critical density. The equilibrium distribution function is expressed as

$$f_\alpha^{\text{eq}} = t_\alpha \rho \left[1 + \frac{e_{\alpha i} u_i}{c_s^2} + \frac{\left(e_{\alpha i} e_{\alpha j} - c_s^2 \delta_{ij}\right) u_i u_j}{2c_s^4} \right], \tag{4}$$

where the weighting factor t_α is given in the following table for d-dimensional b velocity $DdQb$ models for the sake of self-containedness. Table 1 summarizes $DdQb$ lattice models [32].

2.2. Discrete Boltzmann equation for non-ideal gases

Eq. (3) recovers the macroscopic mass and momentum equations

$$\frac{\partial \rho}{\partial t} + \frac{\partial(\rho u_i)}{\partial x_i} = 0, \tag{5}$$

$$\frac{\partial(\rho u_i)}{\partial t} + \frac{\partial\left(\rho u_i u_j\right)}{\partial x_j} = \frac{\partial \sigma_{ij}^{(ig)}}{\partial x_j} + F_i, \tag{6}$$

Table 1
Summary of $DdQb$ lattice models

Model	t_0	t_1	t_2	t_3	t_4	c_s^2
D1Q3	$\frac{2}{3}$	$\frac{1}{6}$	0	0	0	$\frac{1}{3}$
D1Q5	$\frac{1}{2}$	$\frac{1}{6}$	0	0	$\frac{1}{12}$	1
D2Q7	$\frac{1}{2}$	$\frac{1}{12}$	0	0	0	$\frac{1}{4}$
D2Q9	$\frac{4}{9}$	$\frac{1}{9}$	$\frac{1}{36}$	0	0	$\frac{1}{3}$
D2Q13	$\frac{2}{5}$	$\frac{8}{75}$	$\frac{1}{25}$	0	$\frac{1}{300}$	$\frac{2}{5}$
D3Q15	$\frac{2}{9}$	$\frac{1}{9}$	0	$\frac{1}{72}$	0	$\frac{1}{3}$
D3Q19	$\frac{1}{3}$	$\frac{1}{18}$	$\frac{1}{36}$	0	0	$\frac{1}{3}$
D3Q33	$\frac{43}{150}$	$\frac{4}{75}$	$\frac{2}{75}$	$\frac{1}{150}$	$\frac{1}{300}$	$\frac{2}{5}$
D4Q25	$\frac{1}{3}$	0	$\frac{1}{36}$	0	0	$\frac{1}{3}$

where the ideal-gas stress $\sigma_{ij}^{(ig)} = -\rho c_s^2 \delta_{ij} + \mu(\partial_j u_i + \partial_i u_j)$. δ_{ij} is the kronecker δ and μ is the molecular viscosity. F_i represents the intermolecular forcing terms to be defined later. Absence of F_i makes Eq. (6) the ideal-gas Navier–Stokes equations.

To derive an expression for F_i, we consider the momentum equation for non-ideal gases [33]

$$\frac{\partial(\rho u_i)}{\partial t} + \frac{\partial(\rho u_i u_j)}{\partial x_j} = \frac{\partial \sigma_{ij}}{\partial x_j}. \tag{7}$$

The stresses σ_{ij} can be decomposed into three parts: $\sigma_{ij} = -P\delta_{ij} + \sigma_{ij}^{(v)} + \sigma_{ij}^{(1)}$. Here, $P = P(\rho)$ is the thermodynamic pressure for the isothermal fluid and $\sigma_{ij}^{(v)}$ is the viscous stress tensor

$$\sigma_{ij}^{(v)} = \mu\left(\frac{\partial u_i}{\partial x_j} + \frac{\partial u_j}{\partial x_i}\right) - \frac{2}{3}\mu\frac{\partial u_k}{\partial x_k}\delta_{ij}. \tag{8}$$

The second term on the right-hand side is the bulk viscosity term, which is dropped in incompressible fluid. The stress $\sigma_{ij}^{(1)}$ being derived from the Cahn–Hilliard free energy takes the form of

$$\sigma_{ij}^{(1)} = \kappa\left[\left(\frac{1}{2}\frac{\partial \rho}{\partial x_k}\frac{\partial \rho}{\partial x_k} + \rho\frac{\partial^2 \rho}{\partial x_k \partial x_k}\right)\delta_{ij} - \frac{\partial \rho}{\partial x_i}\frac{\partial \rho}{\partial x_j}\right], \tag{9}$$

in which κ is a constant and related to the magnitude of the surface tension.

Comparison of the right-hand sides of Eqs. (6) and (7) suggests that the intermolecular force F_i shall take the form of $F_i = \partial_j \sigma_{ij} - \partial_j \sigma_{ij}^{(ig)}$ [19], and results in

$$F_i = \frac{\partial}{\partial x_j}\left(\rho c_s^2 - P\right)\delta_{ij} + \kappa\frac{\partial}{\partial x_j}\left[\left(\frac{1}{2}\frac{\partial \rho}{\partial x_k}\frac{\partial \rho}{\partial x_k} + \rho\frac{\partial^2 \rho}{\partial x_k \partial x_k}\right)\delta_{ij} - \frac{\partial \rho}{\partial x_i}\frac{\partial \rho}{\partial x_j}\right]. \tag{10}$$

He and coworkers [9,20] chose F_i by considering the intermolecular attraction and the effects of the exclusion volume of the molecules on the equilibrium properties of a dense gas. In either case, the final F_is take the same form.

The thermodynamic pressure P can be determined from the non-ideal gas EOS such as the van der Waals EOS. For the $D2Q9$ lattice model, the van der Waals EOS can be normalized by the critical density ρ_c, the critical temperature T_c, and the reference speed of sound $c_s = 1/\sqrt{3}$ as

$$P_{vw} = \frac{\rho}{3 - \rho} - \frac{3\rho^2}{8T}. \tag{11}$$

P_{vw} is the van der Waals pressure, and ρ and T are normalized density and temperature, respectively. At the critical point, $\rho = 1$ and $T = 1$. Fig. 1 shows a distribution of three regions [34] A, B, and C in a $P - \rho$ diagram, which correspond to the unstable, metastable, and stable regions, respectively. In a van der Waals fluid, the states with $\rho < \rho_\alpha$ are viewed as vapor and the states with $\rho > \rho_\beta$ are viewed as liquid. If $T < 1$, there exists a mechanically unstable region of negative $\partial_\rho P$ (region A), which separates liquid and vapor phases of the fluid.

2.3. Stress and potential form of intermolecular forcing terms

The surface tension force in the intermolecular forcing terms Eq. (10) can be recast in either a stress form or a potential form by using the vector identity. The stress form is the best form if momentum conservation is important, while the potential form is especially good for flows that go to equilibrium states [35]. In the present study, two-distribution function LBE method is developed. One distribution function models pressure and momentum, while the other distribution function models order parameter. Since the primary roles of the two-distribution functions differ, the stress and potential forms of the surface tension force can selectively be adopted in accordance with the purpose of the distribution function.
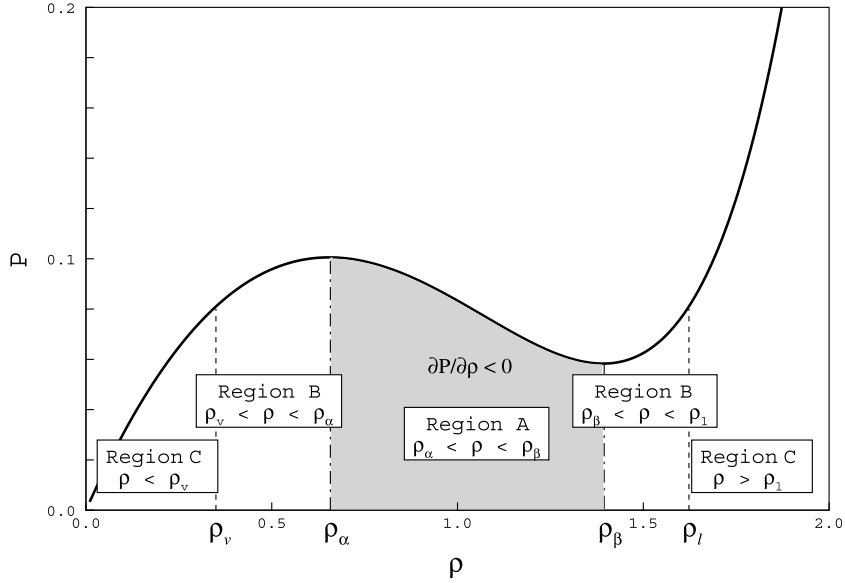
Fig. 1. $P - \rho$ isotherm at $T = 0.9$.

The stress form takes the form of

$$F_i^S = \frac{\partial}{\partial x_j}\left(\rho c_s^2 - p\right)\delta_{ij} + \kappa \frac{\partial}{\partial x_j}\left(\frac{\partial \rho}{\partial x_k}\frac{\partial \rho}{\partial x_k}\delta_{ij} - \frac{\partial \rho}{\partial x_i}\frac{\partial \rho}{\partial x_j}\right), \tag{12}$$

in which the modified pressure is defined as

$$p = P - \kappa\rho\frac{\partial^2 \rho}{\partial x_k \partial x_k} + \frac{\kappa}{2}\frac{\partial \rho}{\partial x_k}\frac{\partial \rho}{\partial x_k}. \tag{13}$$

The second term on the right-hand side of Eq. (12) is the surface tension stress tensor and its principle axes are directed in and perpendicular to the tangent plane of the interface. The normal stress perpendicular to the plane is zero and the two tangent normal stresses are equal. It guarantees that surface tension will not change the total momentum in any volume whose surface is not intersected by interfaces [35]. More importantly, the profile of the modified pressure across the phase interface is smooth compared with that of the pressure in the potential form, which would greatly improves the stability in the case of large surface tension force. Therefore, the stress form shall be used in the DBE/LBE for pressure and momentum. In the later section, the modified pressure in the stress form will be identified as the hydrodynamic pressure.

For the DBE/LBE for order parameter, the potential form of the surface tension force shall be adopted. The potential form is a suitable form when phase separation is important. Furthermore, the equilibrium interface thickness and surface tension can easily be controlled with the potential form. The potential form is derived from Eq. (10) after some algebraic manipulation:

$$F_i^P = \frac{\partial}{\partial x_j}\left(\rho c_s^2 - P\right)\delta_{ij} + \kappa\rho\frac{\partial}{\partial x_i}\frac{\partial^2 \rho}{\partial x_j \partial x_j}. \tag{14}$$

The pressure in the potential form may also be written in a more useful form for the control of interface thickness and surface tension at equilibrium. The thermodynamic relations yield

$$\left(\frac{\partial P}{\partial \rho}\right)_{\mathrm{T}} = \rho \left(\frac{\partial \varphi}{\partial \rho}\right)_{\mathrm{T}}, \tag{15}$$

where P is related to the free energy E_{f} by

$$P = \rho \left(\frac{\partial E_{\mathrm{f}}}{\partial \rho}\right)_{\mathrm{T}} - E_{\mathrm{f}}, \tag{16}$$

and φ is the chemical potential and defined by the derivative of the free energy with respect to the density

$$\varphi = \left(\frac{\partial E_{\mathrm{f}}}{\partial \rho}\right)_{\mathrm{T}}. \tag{17}$$

From Eq. (15) it follows

$$\frac{\partial P}{\partial x_i} = \rho \frac{\partial \varphi}{\partial x_i}. \tag{18}$$

Using this thermodynamic identity, Eq. (14) can be recast as

$$F_i^{\mathrm{P}} = \frac{\partial \rho c_{\mathrm{s}}^2}{\partial x_j} \delta_{ij} - \rho \frac{\partial}{\partial x_i} \left(\varphi - \kappa \frac{\partial^2 \rho}{\partial x_j \partial x_j}\right). \tag{19}$$

The Cahn–Hilliard diffusion drives the total energy toward a minimum and tends to maintain the profile $\varphi^{\mathrm{eq}} = 0$, where

$$\varphi^{\mathrm{eq}} = \varphi - \kappa \frac{\partial^2 \rho}{\partial x_k \partial x_k}. \tag{20}$$

2.4. Discrete Boltzmann equation for pressure and momentum

In this section, the DBE for mass and momentum Eq. (3) is transformed into the DBE for hydrodynamic pressure and momentum. This transform eliminates acoustic waves from two-phase DBE in the low frequency limit and improves stability. In order to perform the transformation, we define a new particle distribution function [9,19]:

$$g_\alpha = f_\alpha + \left(\frac{p}{c_{\mathrm{s}}^2} - \rho\right) \Gamma_\alpha(0), \tag{21}$$

where

$$\Gamma_\alpha(\mathbf{u}) = t_\alpha \left[1 + \frac{e_{\alpha i} u_i}{c_{\mathrm{s}}^2} + \frac{(e_{\alpha i} e_{\alpha j} - c_{\mathrm{s}}^2 \delta_{ij}) u_i u_j}{2 c_{\mathrm{s}}^4}\right]. \tag{22}$$

Taking the total derivative Dt of the new variable g_α gives

$$\begin{aligned}
\frac{D g_\alpha}{Dt} &= \frac{D f_\alpha}{Dt} + \frac{1}{c_{\mathrm{s}}^2} \frac{Dp}{Dt} \Gamma(0) - \frac{D\rho}{Dt} \Gamma(0) \\
&= -\frac{1}{\lambda} \left(g_\alpha - g_\alpha^{\mathrm{eq}}\right) + \frac{(e_{\alpha i} - u_i) \partial_i \left(\rho c_{\mathrm{s}}^2 - p\right)}{c_{\mathrm{s}}^2} \left(\Gamma_\alpha(\mathbf{u}) - \Gamma_\alpha(0)\right) \\
&\quad + \frac{(e_{\alpha i} - u_i) \left[\kappa \partial_i (\partial_k \rho \partial_k \rho) - \kappa \partial_j \left(\partial_i \rho \partial_j \rho\right)\right]}{c_{\mathrm{s}}^2} \Gamma_\alpha(\mathbf{u}),
\end{aligned} \tag{23}$$

where the new equilibrium g_α^{eq} reads

$$g_\alpha^{eq} = t_\alpha \left[\frac{p}{c_s^2} + \rho \left(\frac{e_{\alpha i} u_i}{c_s^2} + \frac{\left(e_{\alpha i} e_{\alpha j} - c_s^2 \delta_{ij} \right) u_i u_j}{2 c_s^4} \right) \right], \tag{24}$$

and the stress form of the surface tension force is adopted. Derivation of Eq. (23) requires the continuity equation and the divergence free condition, i.e., $\partial_i u_i = 0$, as follows [9].

$$\frac{1}{c_s^2} \frac{Dp}{Dt} \Gamma(0) = \frac{(e_{\alpha i} - u_i)}{c_s^2} \frac{\partial p}{\partial x_i} \Gamma(0), \tag{25}$$

and

$$\frac{D\rho}{Dt} \Gamma(0) = (e_{\alpha i} - u_i) \frac{\partial \rho}{\partial x_i} \Gamma(0). \tag{26}$$

In the simulation of the lattice Boltzmann fluids, low speed, low Mach number flows are of primary interest. Asymptotic analysis shows that at low Mach numbers, the pressure can be split into two parts: the thermodynamic pressure which is uniform in space and the hydrodynamic pressure which is several orders of magnitude smaller than the thermodynamic pressure [24,25]. Since the thermodynamic pressure is assumed uniform in space, the pressure p defined in Eq. (13) can be considered the hydrodynamic pressure. Dimensional analysis shows that if the hydrodynamic pressure is normalized to ρU_0^2, where U_0 is the characteristic velocity of the system, $\partial_i p \sim \mathcal{O}(Ma^2)$. Thus, the low Mach number approximation states that

$$\frac{(e_{\alpha i} - u_i) \partial_i p}{c_s^2} \left(\Gamma_\alpha(\mathbf{u}) - \Gamma_\alpha(0) \right) \sim \mathcal{O}(Ma^3), \tag{27}$$

which is the same as the order of principal truncation errors in LBE and will be omitted from Eq. (23). Stability is expected to be enhanced since the contribution of $\partial_i \rho c_s^2$ would become at most O($\mathbf{u}$) due to $\Gamma(\mathbf{u}) - \Gamma(0) \sim \mathcal{O}(\mathbf{u})$, and so is the discretization error. This approximation also enables the elimination of acoustic waves in the low frequency limit [36].

The macroscopic equations recovered through the Chapman–Enskog expansion are

$$\frac{1}{\rho c_s^2} \frac{\partial p}{\partial t} + \frac{\partial u_i}{\partial x_i} = 0, \tag{28}$$

$$\rho \left(\frac{\partial u_i}{\partial t} + u_j \frac{\partial u_i}{\partial x_j} \right) = -\frac{\partial p}{\partial x_i} + \frac{\partial}{\partial x_j} \left[\mu \left(\frac{\partial u_i}{\partial x_j} + \frac{\partial u_j}{\partial x_i} \right) \right] + \kappa \left[\frac{\partial}{\partial x_i} \left(\frac{\partial \rho}{\partial x_k} \frac{\partial \rho}{\partial x_k} \right) - \frac{\partial}{\partial x_j} \left(\frac{\partial \rho}{\partial x_i} \frac{\partial \rho}{\partial x_j} \right) \right]. \tag{29}$$

In the low-frequency limit, the divergence-free condition of velocity is approximately satisfied. Note that the low Mach number approximation only applies to the DBE for pressure and momentum equation, not to the DBE for order parameter equation to ensure phase separation.

2.5. Discrete Boltzmann equation for order parameter

Now that the DBE for mass and momentum has been transformed into the DBE for hydrodynamic pressure and momentum, another set of distribution function for order parameter, viz., density, is needed. For this purpose, Eq. (3) with the potential form of the surface tension force suffices, because the potential form is better suited for separating phase interface.

The DBE for order parameter is expressed as

$$\frac{\partial f_\alpha}{\partial t} + e_{\alpha i} \frac{\partial f_\alpha}{\partial x_i} = -\frac{1}{\lambda} \left(f_\alpha - f_\alpha^{eq} \right) + \frac{(e_{\alpha i} - u_i) \left[\partial_i \rho c_s^2 - \rho \partial_i \left(\varphi - \kappa \partial_j^2 \rho \right) \right]}{c_s^2} \Gamma_\alpha(\mathbf{u}). \tag{30}$$

In the vicinity of the critical point, simplification of EOS can be made [37] for the control of interface thickness and surface tension at equilibrium. In this case, we assume that the energy E_f takes the following form [18]:

$$E_f(\rho) \approx \beta(\rho - \rho_v^{sat})^2(\rho - \rho_l^{sat})^2, \tag{31}$$

where β is a constant, and ρ_v^{sat} and ρ_l^{sat} are the densities of vapor and liquid phases at saturation, respectively. Differentiation of Eq. (31) yields the chemical potential

$$\varphi(\rho) \approx 4\beta(\rho - \rho_v^{sat})(\rho - \rho_l^{sat})(\rho - \rho_m), \tag{32}$$

in which $\rho_m = (\rho_v^{sat} + \rho_l^{sat})/2$.

The Cahn–Hilliard free energy was originally derived to describe the near-critical behavior of mixtures, when the density gradients are small. However, it is generally suggested to be even when the density gradients become large [38]. In a plane interface at equilibrium, the density profile across the interface at equilibrium is

$$\rho(z) = \frac{\rho_l^{sat} + \rho_v^{sat}}{2} + \frac{\rho_l^{sat} - \rho_v^{sat}}{2}\tanh\left(\frac{2z}{D}\right), \tag{33}$$

where the interface thickness D is

$$D = \frac{4}{(\rho_l^{sat} - \rho_v^{sat})}\sqrt{\frac{\kappa}{2\beta}}. \tag{34}$$

The surface tension force σ is given by

$$\sigma = \frac{\left(\rho_l^{sat} - \rho_v^{sat}\right)^3}{6}\sqrt{2\kappa\beta}. \tag{35}$$

Thus, the interface thickness at equilibrium is proportional to $\sqrt{\kappa/\beta}$ and its surface tension is proportional to $\sqrt{\kappa\beta}$. The interface thickness is now a numerical parameter as in Jaqmin [35]. The original EOS of the bulk phase is modified, which may effect the thermodynamics of the system. Since the fluids are supposed to be incompressible, the issue of maintaining EOS does not exist in the present LBE model.

The macroscopic governing equation recovered from Eq. (30) with divergence free velocity field is [19]

$$\frac{\partial \rho}{\partial t} + u_i\frac{\partial \rho}{\partial x_i} = \frac{\partial}{\partial x_j}\left[\lambda\left(\frac{\partial P}{\partial x_j} - \frac{\partial p}{\partial x_j}\right)\right], \tag{36}$$

in which the terms on the right-hand side originate from difference between the thermodynamic and hydrodynamic pressure. In the case of negligible hydrodynamic pressure gradient, Eq. (36) becomes

$$\frac{\partial \rho}{\partial t} + u_i\frac{\partial \rho}{\partial x_i} = \frac{\partial}{\partial x_j}\left(\lambda\rho\frac{\partial \varphi}{\partial x_j}\right), \tag{37}$$

in which $\lambda\rho = \mu/c_s^2$ acts as the mobility in the Cahn–Hilliard equation with advection [29,35].

3. Discretization

3.1. Two-distribution lattice Boltzmann equation

In order to solve DBEs derived in the previous sections, these equations are discretized along characteristics over time step δt. The LBE for g_α thus obtained is

$$g_\alpha(\mathbf{x} + \mathbf{e}_\alpha \delta t, t + \delta t) - g_\alpha(\mathbf{x}, t) = -\int_t^{t+\delta t} \frac{g_\alpha - g_\alpha^{\mathrm{eq}}}{\lambda}\,\mathrm{d}t + \int_t^{t+\delta t} \frac{(e_{\alpha i} - u_i)\partial_i \rho c_s^2}{c_s^2}[\Gamma_\alpha(\mathbf{u}) - \Gamma_\alpha(0)]\,\mathrm{d}t$$
$$+ \int_t^{t+\delta t} \frac{(e_{\alpha i} - u_i)\left[\kappa \partial_i(\partial_k \rho \partial_k \rho) - \kappa \partial_j(\partial_i \rho \partial_j \rho)\right]}{c_s^2} \Gamma_\alpha(\mathbf{u})\,\mathrm{d}t. \tag{38}$$

Here, the time integration in $[t, t + \delta t]$ is coupled with the space integration in $[\mathbf{x}, \mathbf{x} + \mathbf{e}_\alpha \delta t]$. The Chapman–Enskog analysis shows that the trapezoidal rule must be used for integration in order not to introduce any spurious derivatives into the system while retaining second-order accuracy. Application of the trapezoidal rule leads to

$$g_\alpha(\mathbf{x} + \mathbf{e}_\alpha \delta t, t + \delta t) - g_\alpha(\mathbf{x}, t) = -\left.\frac{g_\alpha - g_\alpha^{\mathrm{eq}}}{2\tau}\right|_{(\mathbf{x},t)} - \left.\frac{g_\alpha - g_\alpha^{eq}}{2\tau}\right|_{(\mathbf{x}+\mathbf{e}_\alpha\delta t, t+\delta t)}$$
$$+ \left.\frac{\delta t}{2} \frac{(e_{\alpha i} - u_i)\partial_i \rho c_s^2}{c_s^2}[\Gamma_\alpha(\mathbf{u}) - \Gamma_\alpha(0)]\right|_{(\mathbf{x},t)}$$
$$+ \left.\frac{\delta t}{2} \frac{(e_{\alpha i} - u_i)\partial_i \rho c_s^2}{c_s^2}[\Gamma_\alpha(\mathbf{u}) - \Gamma_\alpha(0)]\right|_{(\mathbf{x}+\mathbf{e}_\alpha\delta t, t+\delta t)}$$
$$+ \left.\frac{\delta t}{2} \frac{(e_{\alpha i} - u_i)\left[\kappa \partial_i(\partial_k \rho \partial_k \rho) - \kappa \partial_j(\partial_i \rho \partial_j \rho)\right]}{c_s^2} \Gamma_\alpha(\mathbf{u})\right|_{(\mathbf{x},t)}$$
$$+ \left.\frac{\delta t}{2} \frac{(e_{\alpha i} - u_i)\left[\kappa \partial_i(\partial_k \rho \partial_k \rho) - \kappa \partial_j(\partial_i \rho \partial_j \rho)\right]}{c_s^2} \Gamma_\alpha(\mathbf{u})\right|_{(\mathbf{x}+\mathbf{e}_\alpha\delta t, t+\delta t)}, \tag{39}$$

where $\tau = \lambda/\delta t$. Likewise, the LBE for f_α is

$$f_\alpha(\mathbf{x} + \mathbf{e}_\alpha \delta t, t + \delta t) - f_\alpha(\mathbf{x}, t) = -\left.\frac{f_\alpha - f_\alpha^{\mathrm{eq}}}{2\tau}\right|_{(\mathbf{x},t)} - \left.\frac{f_\alpha - f_\alpha^{\mathrm{eq}}}{2\tau}\right|_{(\mathbf{x}+\mathbf{e}_\alpha\delta t, t+\delta t)}$$
$$+ \left.\frac{\delta t}{2} \frac{(e_{\alpha i} - u_i)\left[\partial_i \rho c_s^2 - \rho \partial_i\left(\varphi - \kappa \partial_j^2 \rho\right)\right]}{c_s^2} \Gamma_\alpha(\mathbf{u})\right|_{(\mathbf{x},t)}$$
$$+ \left.\frac{\delta t}{2} \frac{(e_{\alpha i} - u_i)\left[\partial_i \rho c_s^2 - \rho \partial_i\left(\varphi - \kappa \partial_j^2 \rho\right)\right]}{c_s^2} \Gamma_\alpha(\mathbf{u})\right|_{(\mathbf{x}+\mathbf{e}_\alpha\delta t, t+\delta t)}. \tag{40}$$

The above LBEs can be solved in three steps:

Pre-streaming collision step.

$$\bar{g}_\alpha(\mathbf{x}, t) = g_\alpha(\mathbf{x}, t) - \left.\frac{1}{2\tau}\left(g_\alpha - g_\alpha^{\mathrm{eq}}\right)\right|_{(\mathbf{x},t)} + \left.\frac{\delta t}{2} \frac{(e_{\alpha i} - u_i)\partial_i \rho c_s^2}{c_s^2}[\Gamma_\alpha(\mathbf{u}) - \Gamma_\alpha(0)]\right|_{(\mathbf{x},t)}$$
$$+ \left.\frac{\delta t}{2} \frac{(e_{\alpha i} - u_i)\left[\kappa \partial_i(\partial_k \rho \partial_k \rho) - \kappa \partial_j(\partial_i \rho \partial_j \rho)\right]}{c_s^2} \Gamma_\alpha(\mathbf{u})\right|_{(\mathbf{x},t)}, \tag{41}$$

$$\bar{f}_\alpha(\mathbf{x}, t) = f_\alpha(\mathbf{x}, t) - \left.\frac{1}{2\tau}\left(f_\alpha - f_\alpha^{\mathrm{eq}}\right)\right|_{(\mathbf{x},t)} + \left.\frac{\delta t}{2} \frac{(e_{\alpha i} - u_i)\left[\partial_i \rho c_s^2 - \rho \partial_i\left(\varphi - \kappa \partial_k^2 \rho\right)\right]}{c_s^2} \Gamma_\alpha(\mathbf{u})\right|_{(\mathbf{x},t)}. \tag{42}$$

Streaming step.

$$\bar{g}_\alpha(\mathbf{x} + \mathbf{e}_\alpha\delta t, t + \delta t) = \bar{g}_\alpha(\mathbf{x}, t), \tag{43}$$

$$\bar{f}_\alpha(\mathbf{x} + \mathbf{e}_\alpha\delta t, t + \delta t) = \bar{f}_\alpha(\mathbf{x}, t). \tag{44}$$

Post-streaming collision step.

$$g_\alpha(\mathbf{x} + \mathbf{e}_\alpha\delta t, t + \delta t) = \bar{g}_\alpha(\mathbf{x} + \mathbf{e}_\alpha\delta t, t + \delta t) - \frac{1}{2\tau + 1}\left(\bar{g}_\alpha - g_\alpha^{\mathrm{eq}}\right)\Big|_{(\mathbf{x}+\mathbf{e}_\alpha\delta t, t+\delta t)}$$
$$+ \frac{2\tau}{2\tau + 1}\frac{\delta t}{2}\frac{(e_{\alpha i} - u_i)\partial_i\rho c_s^2}{c_s^2}[\Gamma_\alpha(\mathbf{u}) - \Gamma_\alpha(0)]\Big|_{(\mathbf{x}+\mathbf{e}_\alpha\delta t, t+\delta t)}$$
$$+ \frac{2\tau}{2\tau + 1}\frac{\delta t}{2}\frac{(e_{\alpha i} - u_i)\left[\kappa\partial_i(\partial_k\rho\partial_k\rho) - \kappa\partial_j(\partial_i\rho\partial_j\rho)\right]}{c_s^2}\Gamma_\alpha(\mathbf{u})\Big|_{(\mathbf{x}+\mathbf{e}_\alpha\delta t, t+\delta t)}, \tag{45}$$

$$f_\alpha(\mathbf{x} + \mathbf{e}_\alpha\delta t, t + \delta t) = \bar{f}_\alpha(\mathbf{x} + \mathbf{e}_\alpha\delta t, t + \delta t) - \frac{1}{2\tau + 1}\left(\bar{f}_\alpha - f_\alpha^{\mathrm{eq}}\right)\Big|_{(\mathbf{x}+\mathbf{e}_\alpha\delta t, t+\delta t)}$$
$$+ \frac{2\tau}{2\tau + 1}\frac{\delta t}{2}\frac{(e_{\alpha i} - u_i)\left[\partial_i\rho c_s^2 - \rho\partial_i\left(\varphi - \kappa\partial_k^2\rho\right)\right]}{c_s^2}\Gamma_\alpha(\mathbf{u})\Big|_{(\mathbf{x}+\mathbf{e}_\alpha\delta t, t+\delta t)}. \tag{46}$$

The density, the velocity, and the hydrodynamic pressure are calculated below after the streaming step.

$$\rho = \sum_\alpha \bar{f}_\alpha, \tag{47}$$

$$\rho u_i = \sum_\alpha \mathbf{e}_\alpha\bar{g}_\alpha + \frac{\delta t}{2}\kappa\left[\frac{\partial}{\partial x_i}\left(\frac{\partial\rho}{\partial x_k}\frac{\partial\rho}{\partial x_k}\right) - \frac{\partial}{\partial x_j}\left(\frac{\partial\rho}{\partial x_i}\frac{\partial\rho}{\partial x_j}\right)\right], \tag{48}$$

$$p = \sum_\alpha \bar{g}_\alpha + \frac{\delta t}{2}u_i\frac{\partial\rho c_s^2}{\partial x_i}. \tag{49}$$

The pre-streaming collision step and the post-streaming collision step may be combined into a single collision step [9]. We retain the above three-step solution procedure in the present study, since the forcing terms in each collision step require different discretization schemes as will be shown in the next section.

The relaxation time τ is assumed to linearly depend on density in the interface region by the following formula [39]:

$$\tau = C\tau_l - (1 - C)\tau_v, \tag{50}$$

where τ_l and τ_v are the relaxation time for liquid and vapor, respectively. $C = (\rho - \rho_v^{\mathrm{sat}})/(\rho_l^{\mathrm{sat}} - \rho_v^{\mathrm{sat}})$ is the composition. The kinematic viscosity is then available and given by $v = \tau c_s^2\delta t$.

3.2. Discretization of forcing terms

Since the perfect shift in the streaming step provides neither inherent numerical dissipation nor numerical error, the collision steps must contain mechanism for stable solution. Time and space discretizations of the directional derivatives in the intermolecular forcing terms are crucial in this regard. If treated explicitly in time, the directional derivatives pose a severe restriction in time step and grid size as well. For instance, in

the LBE for order parameter, the leading order forcing term is the directional derivative of the density $\mathbf{e}_\alpha \cdot \nabla \rho \Gamma$ and its magnitude is approximately equal to that of the distribution function

$$\mathcal{O}(\mathbf{e}_\alpha \cdot \nabla \rho \Gamma) \approx \mathcal{O}(\mathbf{e}_\alpha \cdot \nabla f_\alpha). \tag{51}$$

Therefore, it is obvious that the explicit treatment of the directional derivative of the density must be avoided. In addition, the space discretization must be smooth enough for stability, and accurate enough to comply with the second-order accuracy of LBE. Low order discretizations deteriorate the accuracy of LBE and high order discretizations could generate unwanted oscillations. In this section, the implicit time marching scheme for discretization of LBE is presented and the stable and accurate treatment of the inter-molecular forcing terms on a compact computational stencil is developed.

To shed light on discretization of the directional derivatives in LBE, we consider 1-D advection equation with a source term:

$$\frac{\mathrm{d}\phi}{\mathrm{d}t} + e\frac{\mathrm{d}\phi}{\mathrm{d}x} = e\frac{\mathrm{d}S(\phi)}{\mathrm{d}x}, \tag{52}$$

where ϕ can be considered a single velocity particle distribution function, $S(\phi)$ is a function of ϕ, and e is a constant advection velocity. This equation mimics the behavior of DBE without the effects of the collision and higher order terms. For simplicity of analysis, S is assumed to be linearly proportional to ϕ, i.e., $S = k\phi$. In this particular case, the model equation is reduced to the pure advection equation with an advection velocity of $e(1 - k)$. As in the discretization of LBE, the model equation is discretized along characteristics

$$\phi(x + e\delta t, t + \delta t) - \phi(x, t) = \int_t^{t+\delta t} ke\frac{\mathrm{d}\phi}{\mathrm{d}x} \, \mathrm{d}t. \tag{53}$$

Now that the left-hand side of the above equation is free from any numerical error because it is the exact solution of the pure advection equation, the remaining task is to develop discretization schemes for the right-hand side integral. A good discretization scheme should preserve the initial profile of ϕ without generating oscillations during advection process.

Application of the trapezoidal rule leads to

$$\phi(x + e\delta t, t + \delta t) - \phi(x, t) = \frac{ke\delta t}{2} \left(\frac{\mathrm{d}\phi}{\mathrm{d}x}\bigg|_{(x+e\delta t, t+\delta t)} + \frac{\mathrm{d}\phi}{\mathrm{d}x}\bigg|_{(x,t)} \right), \tag{54}$$

which can be solved in three steps as in the case of the LBE method:

Pre-streaming step.

$$\bar{\phi}(x, t) = \phi(x, t) + \frac{ke\delta t}{2} \frac{\mathrm{d}\phi}{\mathrm{d}x}\bigg|_{(x,t)} \tag{55}$$

Streaming step.

$$\bar{\bar{\phi}}(x + e\delta t, t + \delta t) = \bar{\phi}(x, t) \tag{56}$$

Post-streaming step.

$$\phi(x + e\delta t, t + \delta t) - \frac{ke\delta t}{2} \frac{\mathrm{d}\phi}{\mathrm{d}x}\bigg|_{(x+e\delta t, t+\delta t)} = \bar{\bar{\phi}}(x + d\delta t, t + \delta t). \tag{57}$$

The desirable discretization scheme for the directional derivative should be stable and second-order accurate. One popular choice for discretization of the directional derivative is the first-order biased difference [40,41].

3.2.1. First-order biased difference (1B)

$$e\delta t \frac{\mathrm{d}\phi}{\mathrm{d}x}\bigg|_{(x)}^{1B} = \phi(x + e\delta t) - \phi(x). \tag{58}$$

Obviously, this is only first-order accurate and tends to smear any sharp profile. Although LBE can be derived from the first-order biased discretization of DBE with unit *CFL* (Courant–Friedrichs–Lewy) number, it is more general to derive it from second-order central schemes such as the Lax–Wendroff discretization of DBE [28,42]. This is because the Lax–Wendroff discretization of DBE recovers the Navier-Stokes equations up to second-order accuracy for any *CFL* numbers less than or equal to unity, whereas the first-order biased discretization requires *CFL* = 1 to recover the same accurate equations.

Using the second-order central discretization implies that all the terms in DBE must be discretized using the second-order central scheme:

3.2.2. Second-order central difference (2C)

$$e\delta t \frac{\mathrm{d}\phi}{\mathrm{d}x}\bigg|_{(x)}^{2C} = \frac{\phi(x + e\delta t) - \phi(x - e\delta t)}{2}. \tag{59}$$

In addition to second-order accuracy, the second-order central scheme preserves symmetry. The major drawback of the central difference for the directional derivative is its severe dispersion error arising from non-compact computational supports. Viewed from the point $(x + e\delta t, t + \delta t)$, Eq. (54) with the second-order central difference requires four grid points. To get compact discretization, Taylor-series expansion of the derivative around $(x + e\delta t, t)$ could be utilized

$$\frac{\mathrm{d}\phi}{\mathrm{d}x}\bigg|_{(x)} = \left[\frac{\mathrm{d}\phi}{\mathrm{d}x} - e\delta t \frac{\mathrm{d}^2\phi}{\mathrm{d}x^2}\right]_{(x+e\delta t)} + \mathcal{O}(\delta x^2). \tag{60}$$

The first term in the square bracket on the right-hand side is the low-order approximation to the derivative on the left-hand side and the second term on the right-hand side can be considered a correction term. With the second-order central differences for both first and second derivatives, Eq. (60) is written as

3.2.3. Second-order biased difference (2B)

$$e\delta t \frac{\mathrm{d}\phi}{\mathrm{d}x}\bigg|_{(x)}^{2B} = \frac{-\phi(x + 2e\delta t) + 4\phi(x + e\delta t) - 3\phi(x)}{2}. \tag{61}$$

With the second-order biased difference, Eq. (54) is now fully discretized:

$$\phi(x + e\delta t, t + \delta t) - \phi(x,t) = \frac{ke\delta t}{2}\left(\frac{\mathrm{d}\phi}{\mathrm{d}x}\bigg|_{(x+e\delta t, t+\delta t)}^{2C} + \frac{\mathrm{d}\phi}{\mathrm{d}x}\bigg|_{(x,t)}^{2B}\right). \tag{62}$$

Note that the directional derivative at $(x + e\delta t, t + \delta t)$ is discretized using the second-order central scheme for symmetry.

Generally, the second-order central scheme generates oscillations at the leading edge of the wave. While the second-order biased scheme works better, it still signals small undershoot at the trailing edge of the wave. Thus, it is natural to propose a difference scheme that switches computational stencils from the second-order biased discretization to the second-order central discretization when non-smoothness is detected. The second-order mixed scheme is based on this idea.

3.2.4. Second-order mixed difference (2M)

$$
\left.\frac{\mathrm{d}\phi}{\mathrm{d}x}\right|^{2M}_{(x)} = \left.\frac{\mathrm{d}\phi}{\mathrm{d}x}\right|^{2B}_{(x)}, \quad \text{if} \quad \left(\left.\frac{\mathrm{d}\phi}{\mathrm{d}x}\right|^{2B}_{(x)} \times \left.\frac{\mathrm{d}\phi}{\mathrm{d}x}\right|^{2C}_{(x+e\delta t)}\right) \geqslant 0,
$$

$$
\left.\frac{\mathrm{d}\phi}{\mathrm{d}x}\right|^{2M}_{(x)} = \left.\frac{\mathrm{d}\phi}{\mathrm{d}x}\right|^{2C}_{(x)}, \quad \text{if} \quad \left(\left.\frac{\mathrm{d}\phi}{\mathrm{d}x}\right|^{2B}_{(x)} \times \left.\frac{\mathrm{d}\phi}{\mathrm{d}x}\right|^{2C}_{(x+e\delta t)}\right) < 0,
\tag{63}
$$

in which $\mathrm{d}\phi/\mathrm{d}x|^{2C}_{(x+e\delta t)}$ is used as a smoothness indicator. $\mathrm{d}\phi/\mathrm{d}x|^{2C}_{(x+e\delta t)}$ is a low-order approximation to $\mathrm{d}\phi/\mathrm{d}x|^{2C}_{(x)}$ and always produces monotonic profile. If $\mathrm{d}\phi/\mathrm{d}x|^{2C}_{(x+e\delta t)}$ has a different sign from $\mathrm{d}\phi/\mathrm{d}x|^{2B}_{(x)}$, the computational stencil simply slides to $\mathrm{d}\phi/\mathrm{d}x|^{2C}_{(x)}$. Note that the mixed difference is truly second-order accurate, since it only switches computational stencils between second-order accurate discretizations.

Likewise, it is reasonable to apply the second-order biased/mixed difference Eq. (63) in the pre-streaming collision step while the standard central difference Eq. (59) in the post-streaming collision step. It is found that combining the pre-streaming and post-streaming collision steps into one single collision step poses problems. If the second-order central difference is used in the single collision step, the solution becomes unstable as the density ratio increases and the interface thickness decreases. If the second-order biased or mixed difference is exclusively used in the single collision step, the interface tends to smear due to numerical diffusion and asymmetry.

Derivatives other than the directional derivatives can be obtained by taking moments of the 1-D second-order central discretization of the first and second derivatives along characteristics for consistency, although its effect on stability is not critical. Specifically, the first derivative and the second derivative are discretized as follows (See Appendix A):

$$
\frac{\partial \phi}{\partial x_i} = \sum_{\alpha \neq 0} \frac{t_\alpha \mathbf{e}_\alpha \cdot \hat{\mathbf{i}}[\phi(\mathbf{x} + \mathbf{e}_\alpha \delta t) - \phi(\mathbf{x} - \mathbf{e}_\alpha \delta t)]}{2c_s^2 \delta t},
\tag{64}
$$

$$
\frac{\partial^2 \phi}{\partial x_i \partial x_i} = \sum_{\alpha \neq 0} \frac{t_\alpha [\phi(\mathbf{x} + \mathbf{e}_\alpha \delta t) - 2\phi(\mathbf{x}) + \phi(\mathbf{x} - \mathbf{e}_\alpha \delta t)]}{c_s^2 \delta t^2},
\tag{65}
$$

in which $\hat{\mathbf{i}}$ is the unit vector pointing along the i-coordinate axis. Eq. (64) appears in LBE as in the inner product with the velocity vector, which is $\mathcal{O}(Ma)$. Thus, its contribution to the overall truncation error is smaller than the directional derivatives. Eq. (65) is needed to evaluated the potential form of the surface tension force. Extension of the above discretization schemes to 3-D lattice model is straightforward, and examples are given in Appendix A.

4. Numerical test

In this section, various discretization schemes presented in Section (3.2) are tested for the 1-D model equation (52). The computational results will confirm that the mixed scheme produces not only smooth but accurate solutions. Then, droplet test is carried out for validation and verification of the present LBE method. The stress and potential forms of the surface tension force are compared and error analysis is performed. Finally, droplet splashing on a thin liquid film is examined. It is a challenging problem because the fluids have large density and viscosity differences, and the initial condition presents numerical singularity at the impact point. The results will be compared with the existing power-law for the spread factor.
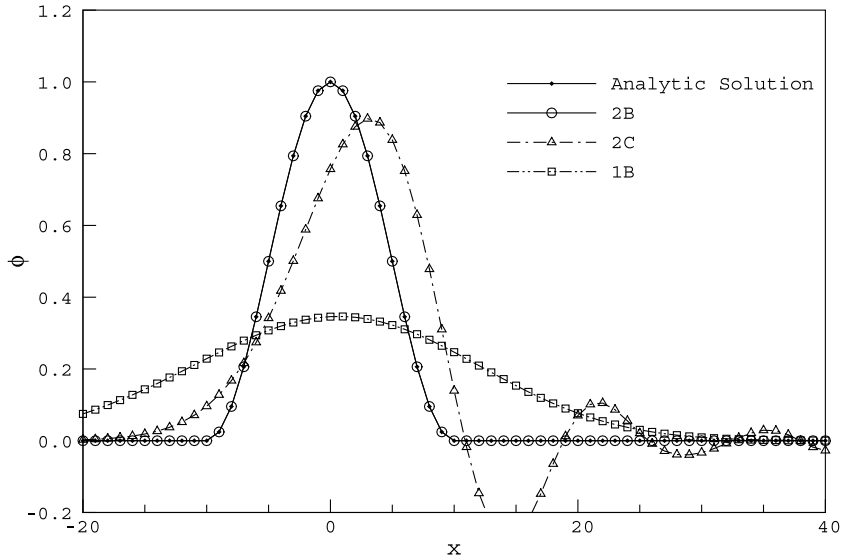
Fig. 2. Solutions of Eq. (52) with $e = 1$, $k = 1.0$ after 120 iterations.

4.1. 1-D Model equation

If S in Eq. (52) is assumed to be $S = k\phi$, the model equation is reduced to the pure advection equation with an advection velocity of $e(1 - k)$

$$\frac{\mathrm{d}\phi}{\mathrm{d}t} + e(1 - k)\frac{\mathrm{d}\phi}{\mathrm{d}x} = 0. \tag{66}$$

Fig. 2 shows the propagation of a sinusoidal wave with various formulations presented in the previous section. If $k = 1.0$, Eq. (66) becomes $\mathrm{d}\phi/\mathrm{d}t = 0$, and the sinusoidal wave must be stationary and retain its initial profile. In the simulation, the width of a single wave is 25 and the results are shown after 120 iterations. The first-order biased difference produces excessive numerical diffusion and the second-order central difference exhibits severe oscillation at the leading edge of the wave. Only the second-order biased difference successfully retains the initial profile and stays at the origin.

In the case of $k = 0.5$ as shown in Fig. 3, the first-order biased difference still produces excessive numerical diffusion even though its amplitude is higher than $k = 1.0$. The second-order central scheme generates oscillations at the leading edge of the wave but the magnitude is smaller than $k = 1.0$. This is because the truncation error of Eq. (52) depends on k. Since the perfect shift is used in the streaming step, both dissipation and dispersion errors decrease as k decreases. The second-order biased scheme works best while it still signals small undershoot at the trailing edge of the wave.

In Figs. 4 and 5, the solutions of the second-order mixed scheme are compared with the solutions of the second-order biased scheme. Clearly, the mixed scheme does not generate wiggles while preserving the initial profile of the sinusoidal wave. It remains second-order accurate over the entire computational domain. To confirm the accuracy of the mixed scheme, a grid convergence test is carried out on successively refined grids. In Fig. 6, all of the second-order schemes presented above are indeed second-order accurate while the first-order biased scheme performs worse than first-order. The second-order mixed scheme gives best results.
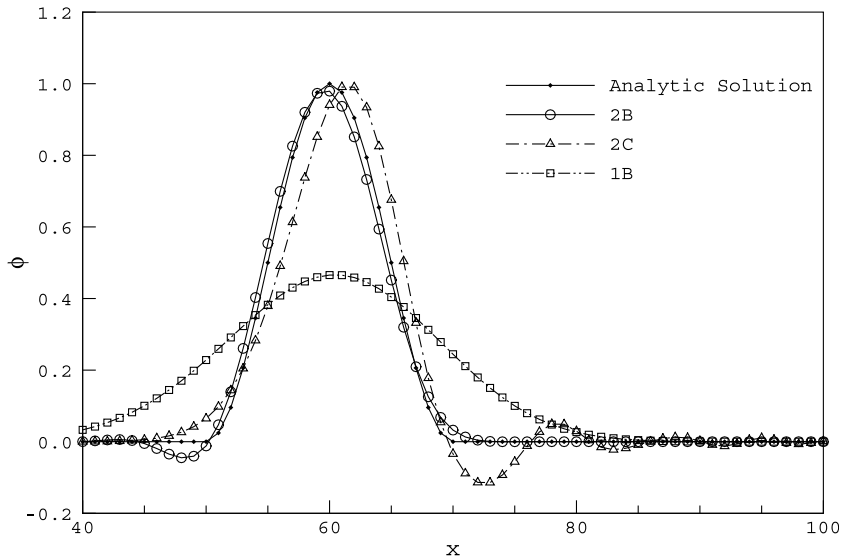
Fig. 3. Solutions of Eq. (52) with $e = 1$, $k = 0.5$ after 120 iterations.
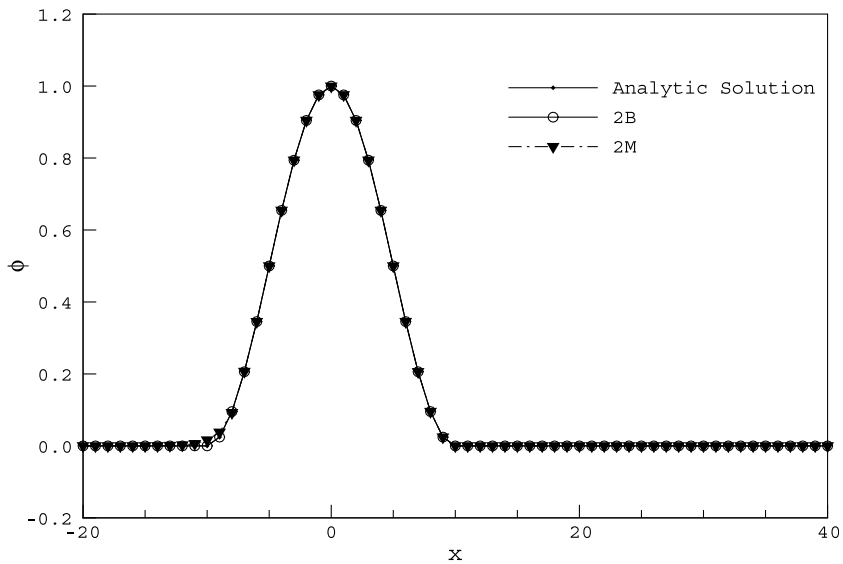
Fig. 4. Solutions of Eq. (52) with $e = 1$, $k = 1.0$ after 120 iterations.

4.2. Stationary droplet

Like the conventional CFD methods, the pressure distribution across the phase interface depends on the surface tension force and is an excellent indicator for numerical stability of the methods. If pressure at the interface exhibits large oscillation, the method tends to be unstable and is restricted to two-phase flows with
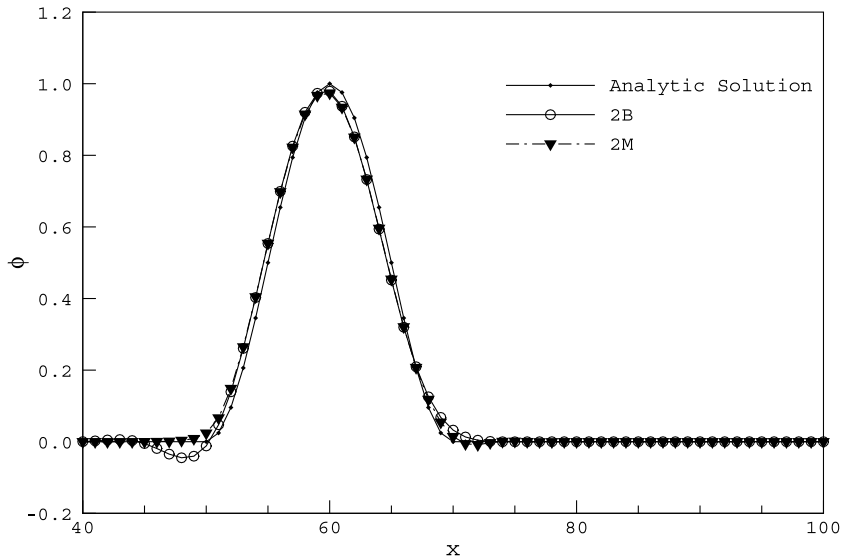
Fig. 5. Solutions of Eq. (52) with $e = 1$, $k = 0.5$ after 120 iterations.
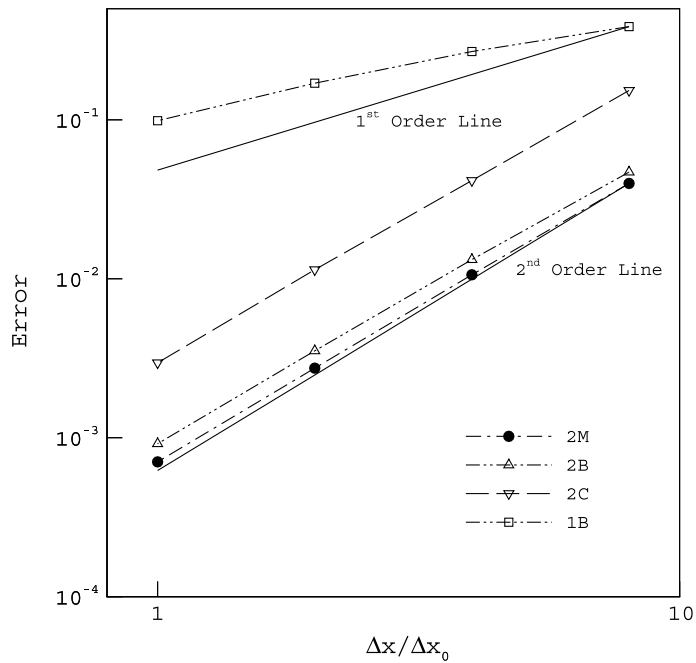
Fig. 6. Error as a function of grid spacing.

small density ratio. In order to evaluate the stress and potential forms of the surface tension force in the LBE for pressure and momentum, Fig. 7 compares the pressure distributions across the interface calculated from both forms. In the LBE for order parameter, the potential form is always used because it is more
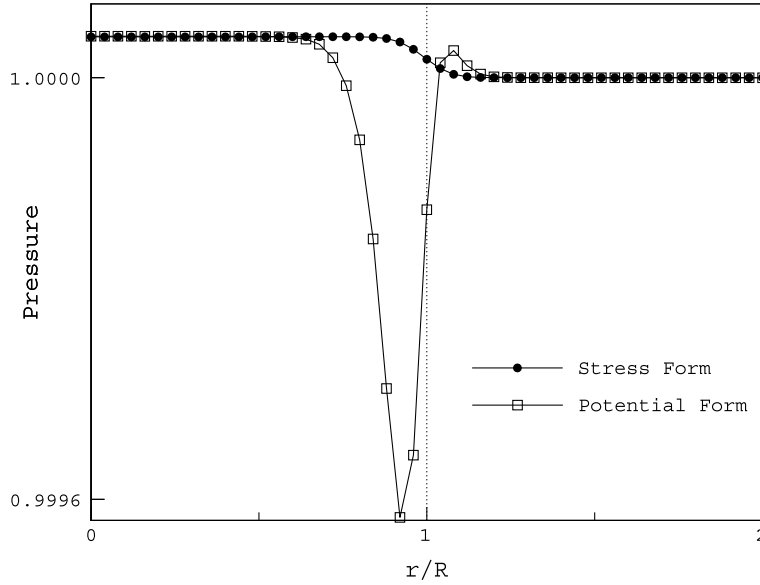
Fig. 7. Pressure distribution on the cross-sectional plane of a droplet. $\sigma = 1.0 \times 10^{-3}$, $D = 5$, and droplet radius $R = 25$. Reference pressure is taken as $p_r = 1$ and $p_i - p_o$ should be 4.0×10^{-5}.

appropriate for phase separation. The results show abrupt changes in the pressure obtained from the potential form, even though this form is still valid and needed for phase separation in the LBE for order parameter. This abrupt change may be one of the reasons for numerical instability restricting previous
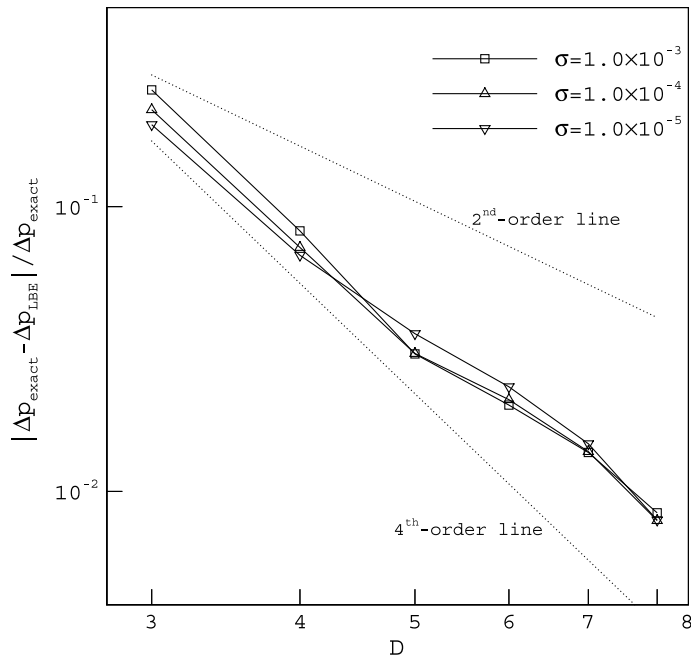
Fig. 8. Convergence of Laplace law as a function of interface thickness D. Droplet radius $R = 25$.

LBE methods from simulating two-phase flow at high density ratio with non-negligible surface tension force. On the contrary, the pressure obtained from the stress form is generally smooth across the interface.

The satisfaction of Laplace law is an important benchmark test. Laplace law states

$$\Delta p = p_{in} - p_{out} = \frac{\sigma}{R}, \tag{67}$$

where p_{in} and p_{out} are the pressures inside and outside the droplet, respectively. Since the surface tension σ is an input parameter for the simulation, the analytic value of Δp_{exact} is computed from Eq. (67), where σ is expressed in Eq. (35) for validation and verification. Understanding the effect of interface thickness D on the solution accuracy is of critical importance in diffuse interface method. As the present LBE method is discretized using second-order differences, a larger D is expected to produce better agreement with the analytic prediction.

Fig. 8 shows the relative error of the measured pressure difference to the analytic pressure difference as a function of the interface thickness D. Δp_{LBE} is measured on nodes that are away from the interface since the values of the pressure vary near the interface (Fig. 7). When the relative error $|\Delta p_{exact} - \Delta p_{LBE}|/|\Delta p_{exact}|$ becomes less than 1.0×10^{-8}, the solution is assumed converged. The result shows that the Laplace law is satisfied, while the agreement with the Laplace law gets better as the interface thickness D increases. It is because the discretization error generally decreases with the interface thickness. It is interesting to note that the convergence rate of the current method is faster than second-order and is hardly dependent on the magnitude of the surface tension. In Fig. 9, the maximum spurious velocity around the droplet is plotted against the interface thickness D. Because the viscosity of the fluid is fixed, the spurious velocity is strong when the surface tension force is large. The spurious velocity diminishes to order of 10^{-7} at $D = 8$ as the interface thickness increases, which can be attributed to reduced discretization error.

A steady state, stationary droplet located at the center of the computational domain must preserve its isotropy, i.e., the equilibrium density profile should be maintained in all directions. Because of discretization
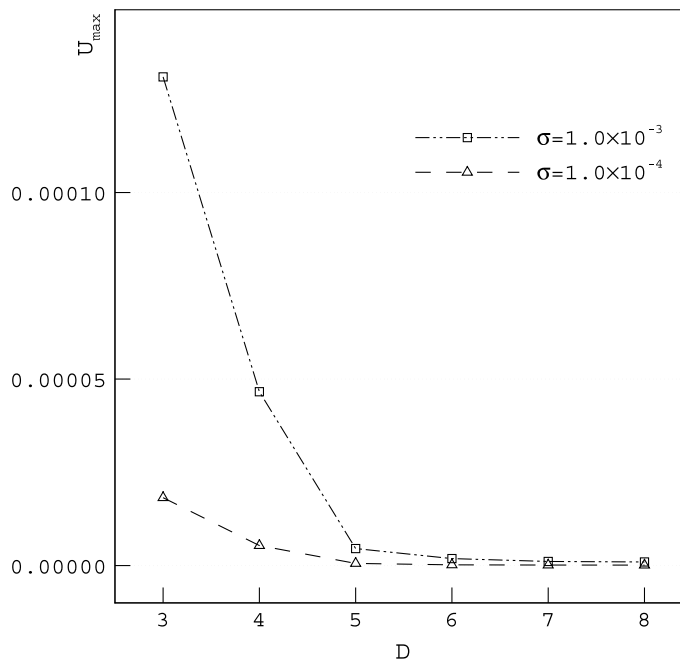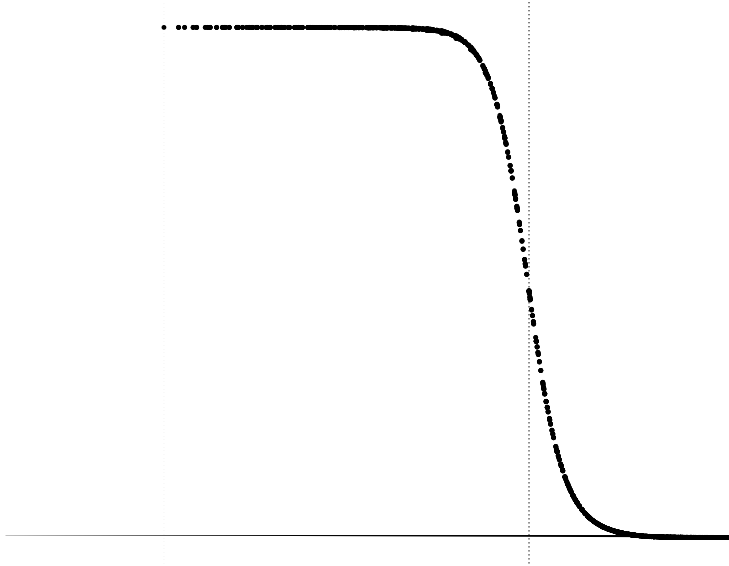

Fig. 9. Maximum spurious velocity as a function of interface thickness D. Droplet radius $R = 25$.

error and grid effect, the isotropy of the solution is not guaranteed in the (CFD) solvers, especially in some upwind-based CFD solvers. The amount of added in the direction neither parallel or perpendicular to the grid is usual deformation of the equilibrium density profile. To test the isotropy of the LBE $D = 5$, the surface tension $\sigma = 1.0 \times 10^{-4}$, and the droplet radius $R = 25$ are parameters are needed to prescribe the initial profile in Eqs. (34) and (35). T is set to 1000 and the relaxation times are $\tau_l = 0.1$ and $\tau_v = 1.0$ for liq 100×100 grid points are used and periodic boundary conditions are imposed. $|\Delta p_{\text{exact}} - \Delta p_{\text{LBE}}|/|\Delta p_{\text{exact}}|$ becomes less than 1.0×10^{-8}, the system is assumed radii of the droplet are examined in all radial directions from the center of the tered density distribution versus the distance from the droplet center is displa single curve, confirming high degree of isotropy of the present LBE model.

4.3. Droplet oscillation

To further assess the accuracy and ability of the present formulation, we e lation using $D3Q19$ lattice model. If an initially spherical droplet is distorted b tion, the droplet starts to exhibit oscillatory behavior between oblate and p According to Lamb [44], the oscillation period for a 3-D inviscid droplet is:

$$T_r = \frac{2\pi}{\sqrt{n(n-1)(n+2)\frac{\sigma}{\rho_l^{\text{sat}} R_0}}},$$

where n is the mode of oscillation and R_0 is the initial radius of droplet.

(a) T/T$_r$ = 0.5 (oblate)

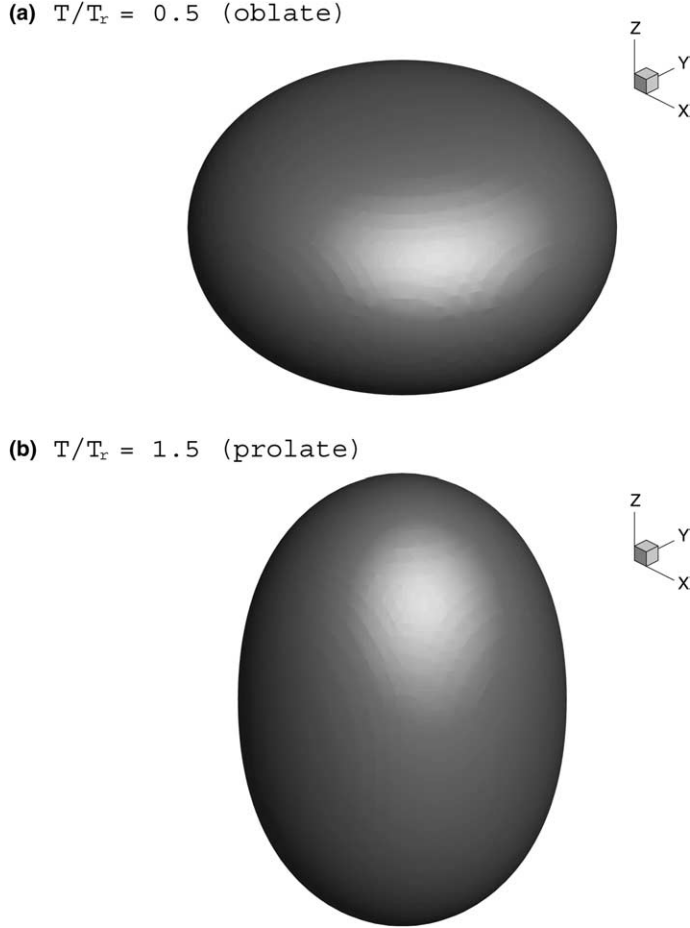**(b)** T/T$_r$ = 1.5 (prolate)

Fig. 11. The shapes of distorted 3-D droplet. (not to scale.)

To introduce the initial perturbation, the following 3-D, axisymmetric velocity field is used.

$$u_i = U_0 x_i / R_0$$
$$u_j = U_0 x_j / R_0 \hspace{6cm} (69)$$
$$u_k = -2U_0 x_k / R_0.$$

This velocity field causes mode 2 perturbation exhibiting the oblate and prolate shapes of the perturbed droplet as in Fig. 11. The prolate distortion is twice the oblate distortion due to mass conservation and axisymmetry.

In the simulation, $U_0 = 5 \times 10^{-4}$ is chosen. The density ratio of two fluids is set to 1000, the surface tension is $\sigma = 2 \times 10^{-3}$, and the relaxation times are $\tau_l = 0.005$ and $\tau_v = 0.05$ for liquid and vapor, respectively. The droplet is initially located at the center of $96 \times 96 \times 96$ grid system and the normal gradient free condition for the particle distribution function is imposed at the domain boundary. Two cases with different initial radii of $R_0 = 24$ and $R_0 = 32$ are compared. It is expected that the droplet with larger radius and thicker interface gives more accurate results. The oscillation period is normalized to the theoretical oscilla-
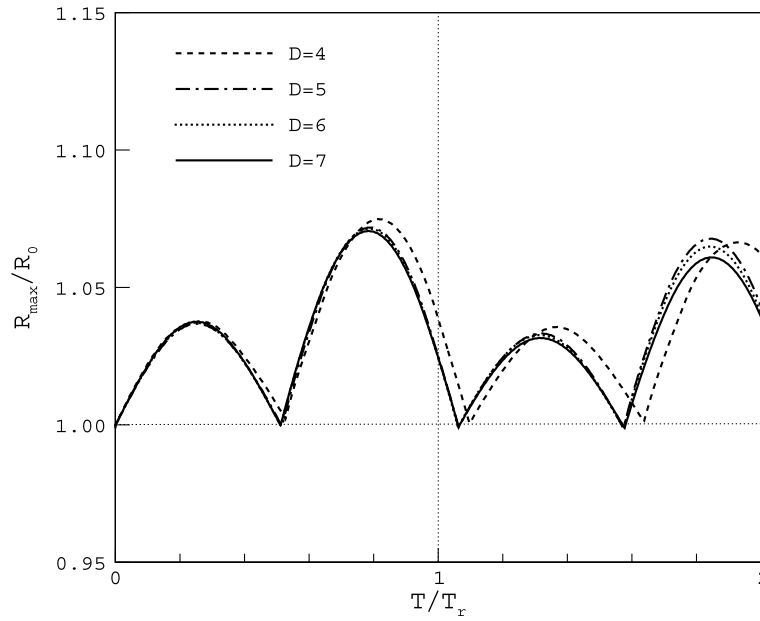
Fig. 12. Ratio between the largest radius and the initial radius with varying interface thickness D. Density ratio $\rho_l/\rho_v = 1000$, viscosity ratio $\mu_l/\mu_g = 100$, drop radius $R = 24$, and surface tension $\sigma = 2.0 \times 10^{-3}$.
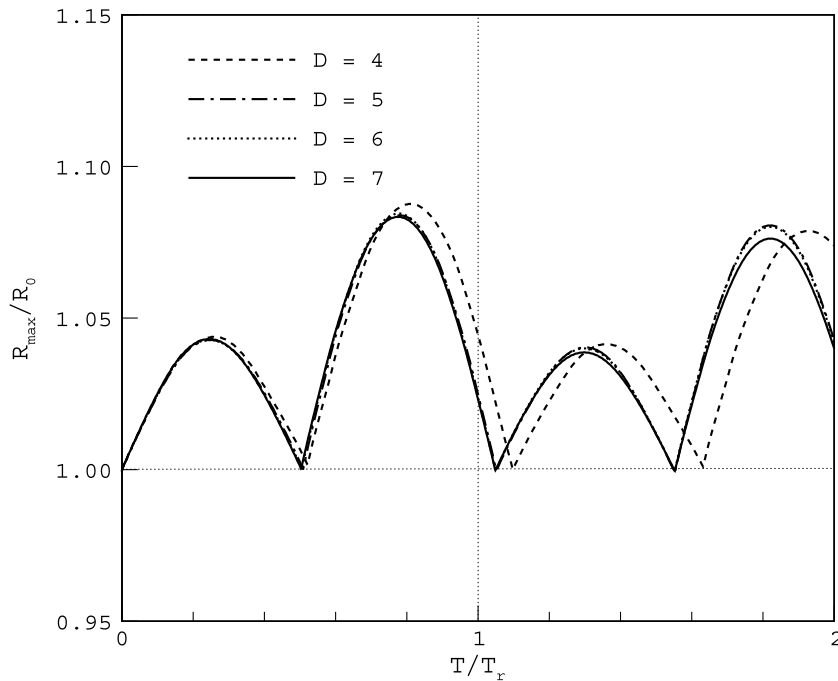

Fig. 13. Ratio between the largest radius and the initial radius with varying interface thickness D. Density ratio $\rho_l/\rho_v = 1000$, viscosity ratio $\mu_l/\mu_g = 100$, drop radius $R = 32$, and surface tension $\sigma = 2.0 \times 10^{-3}$.

Table 2
Normalized period T/T_r[a] of computed 3-D droplet oscillation

Initial radius	$D = 4$	$D = 5$	$D = 6$	$D = 7$
$R_0 = 24$	1.097	1.063	1.061	1.062
$R_0 = 32$	1.098	1.051	1.049	1.048

Density ratio $\rho_l/\rho_v = 1000$, viscosity ratio $\mu_l/\mu_g = 100$, and surface tension $\sigma = 2.0 \times 10^{-3}$.

  [a] $T_r = 5840.3$ and $T_r = 8991.8$ for $R_0 = 24$ and $R_0 = 32$, respectively.

tion period T_r predicted in Eq. (68). The interface thickness D also varies from 4 to 7. In Figs. 12 and 13, the ratio between the largest radius $R_{\max}$ and the initial radius R_0 is plotted against the computed droplet oscillation period T normalized to the theoretical droplet oscillation period T_r with varying interface thickness. As the interface thickness increases, the oscillation period approaches the theoretical value of $T/T_r = 1$. The improvement is most obvious between $D = 4$ and $D = 5$. Table 2 summarizes the oscillation periods for different cases. The percentage error for $R_0 = 32$ and $D > 5$ is less than 5%.

Figs. 12 and 13 also show that the amplitude of oscillation gradually decreases because of viscous effect. It is interesting to note that while the oscillation period is predicted better with larger interface thickness, the amplitude of the oscillation damps faster with larger interface thickness. This is reasonable because the viscosity of the liquid is 100 times bigger than that of the gas in the simulation and thus, the gas phase contains more viscous fluid as the interface thickens.

4.4. Droplet splashing on a thin liquid film

The phenomenon of droplet splashing is found in raindrop splashing on the ground, the impact of fuel droplet on the wall of a combustion chamber, and ink-jet printing. In this section, we concentrate on the early stage of droplet impact on a thin liquid film. We chose this case because it is challenging in that the
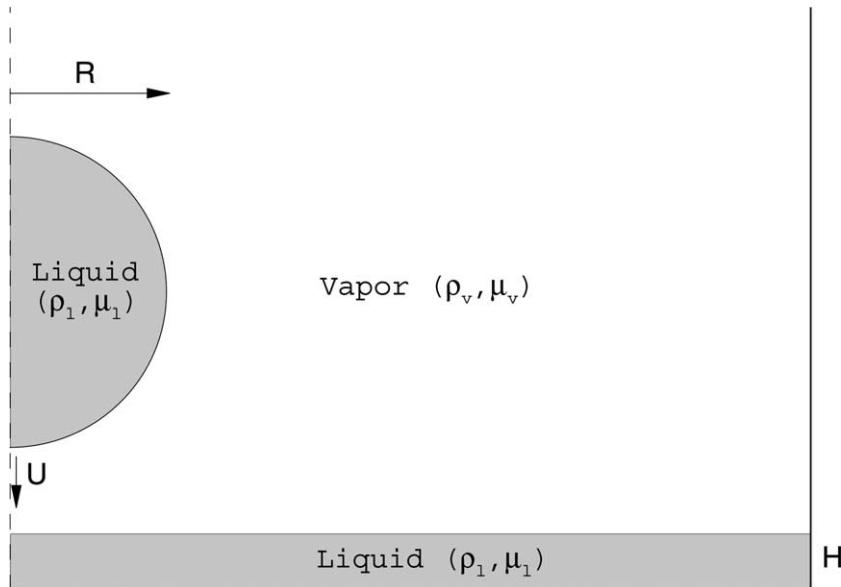

Fig. 14. Schematic representation of the simulation setup for droplet splashing on a thin liquid film.

fluids have large density and viscosity differences, and the initial condition presents numerical singularity at the impact point. In addition, previous research results show that the power law is generally valid at short times after the impact.

Important relevant non-dimensional parameters are the Weber number (We_l) and the Reynolds number (Re_l) based on the properties of liquid:

$$We_l = \frac{2\rho_l U^2 R}{\sigma}, \tag{70}$$

$$Re_l = \frac{2\rho_l U R}{\mu_l}, \tag{71}$$

where U is the velocity of the droplet at the instant of impact, R is the radius of the droplet, and σ is the surface tension. The non-dimensional time is measured by $2R/U$.

Schematic representation of the simulation setup is shown in Fig. 14. Symmetric boundary condition and periodic boundary condition are imposed at the left and right boundaries, respectively. Top boundary is open, for which the second-order extrapolations of all variables are utilized. Initially, potential flow solution is imposed. The density ratio of the liquid phase and the vapor phase is fixed at $\rho_l^{\mathrm{sat}}/\rho_v^{\mathrm{sat}} = 1000$ and the Weber number is set to $We_l = 8{,}000$. Following Josserand and Zaleski [45], the viscosity of the vapor is kept constant such that the Re_l of the flow is determined by the viscosity of the liquid. The least viscous case has a Re_l of 500, which corresponds to the viscosity ratio of $\mu_l/\mu_v = 40$. A series of computations have been carried out with six different Re_l: 20, 100, 200, 300, 400 and 500. The corresponding relaxation time τ_l ranges from 0.006 to 0.15. $U = 0.005$, $R = 100$, and 1000×500 grid points are used. This choice of the number of grid points and the diameter is determined by the minimum allowable relaxation time for the liquid phase, which is found to be $\tau_l > 0.005$. It is well known that as τ_l approaches zero, the LBE scheme becomes unstable [28]. Dimensional analysis dictates that the effects of compressibility and gravity are negligible [45].

Previous research works indicate that there are two possible outcomes resulting from the impact process: splashing and deposition. For strong impacts with large We_l, a velocity jet is formed in the vapor phase at the neck region where the drop and the film meet [46]. If Re_l is high enough, a thin liquid sheet is emitted immediately after the impact, which grows into a corolla and propagates outward away from the drop. The end rim that grows at the edge of the corolla is unstable and develops fingers of liquid [47]. The fingers eventually break up into small droplets by the Rayleigh–Plateau instability. The spread radius r generally follows the $r \sim \sqrt{t}$ spreading law. This process is called splashing. If Re_l is small, the drop only spreads gently on the surface without emitting the liquid sheet. This process is called deposition.

Figs. 15–17 show the time evolutions of the droplet and the thin liquid film after the instant of impact, at which the non-dimensional time $Ut/2R$ is set to zero. In these figures, the interface is represented by 10 equally spaced contour levels between ρ_α and ρ_β. As mentioned in Section 2 and illustrated in Fig. 1, the states with $\rho < \rho_\alpha$ are viewed as vapor and the states with $\rho > \rho_\beta$ are viewed as liquid. For the cases of $Re_l = 500$ and $Re_l = 100$, splashing is observed. In contrast, for $Re_l = 20$ case, the impact does not result in splashing but an outward moving surface wave, thus being a deposition process. Immediately after the impact, small vapor bubbles are entrapped in the phase interface region (Figs. 15–17(c) and (d)). The entrapped vapor bubbles eventually undergo phase change and are absorbed into liquid. Physical implication of this phenomena requires further study because unlike previous research works based on either potential flow model [46] or viscous flow model [45], the present LBE model allows phase change due to pressurization/depressurization.

A close-up view of the interface shapes ($\rho = \rho_m$) and the velocity vectors for $Re_l = 500$ in the neck region is provided in Fig. 18. Fig. 18(a) shows interface shapes at different non-dimensional time with the interval
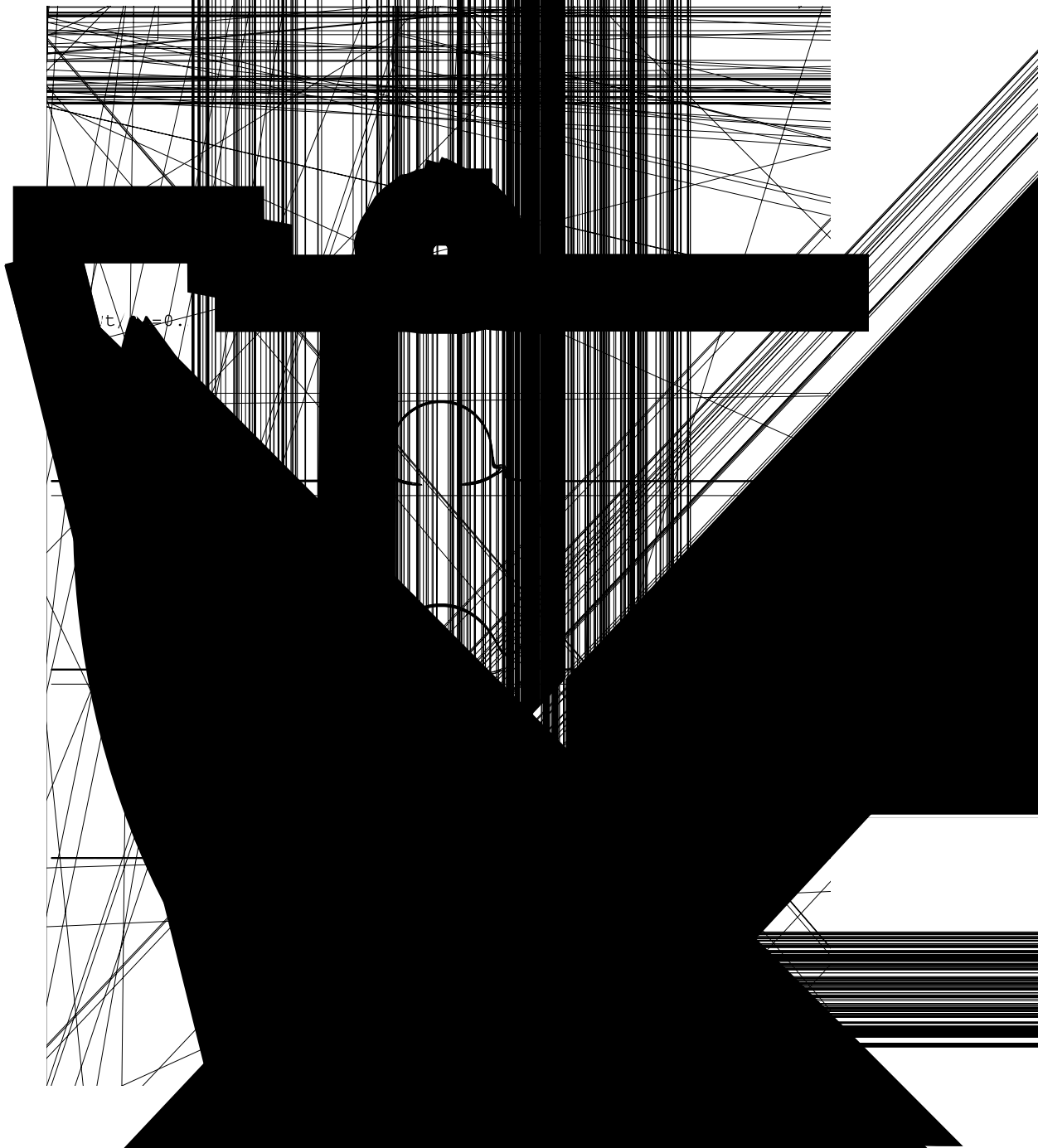
of $Ut/2R = 0.1$ b ... eck is clearly ob-
served. The en ... typical velocity
jet associat ... tor $r/2R$ for
$Re_1 = 100$ ... n of ... straight line

(a) $Ut/2R=0.0$

(b) $Ut/2R=0.1$
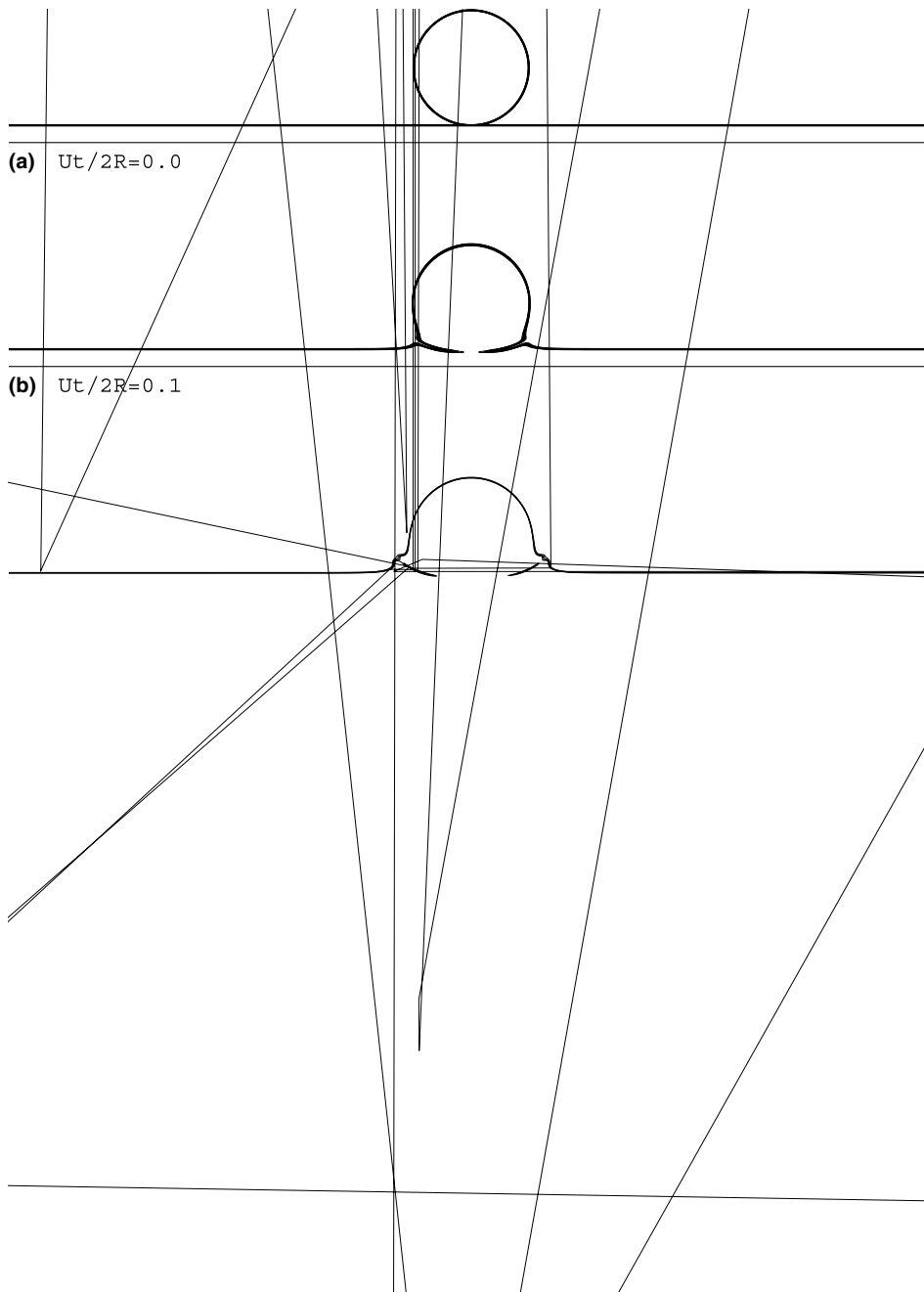
corresponds to the power law $r = \sqrt{2RUt}$. The power law is generally valid at short times after the impact. Overall the numerical solutions obey the power law. As Josserand and Zaleski [45] noted, no significant dependence on the viscosity is found. Slight deviation from the straight line is observed for $Ut/2R \leqslant 0.06$,
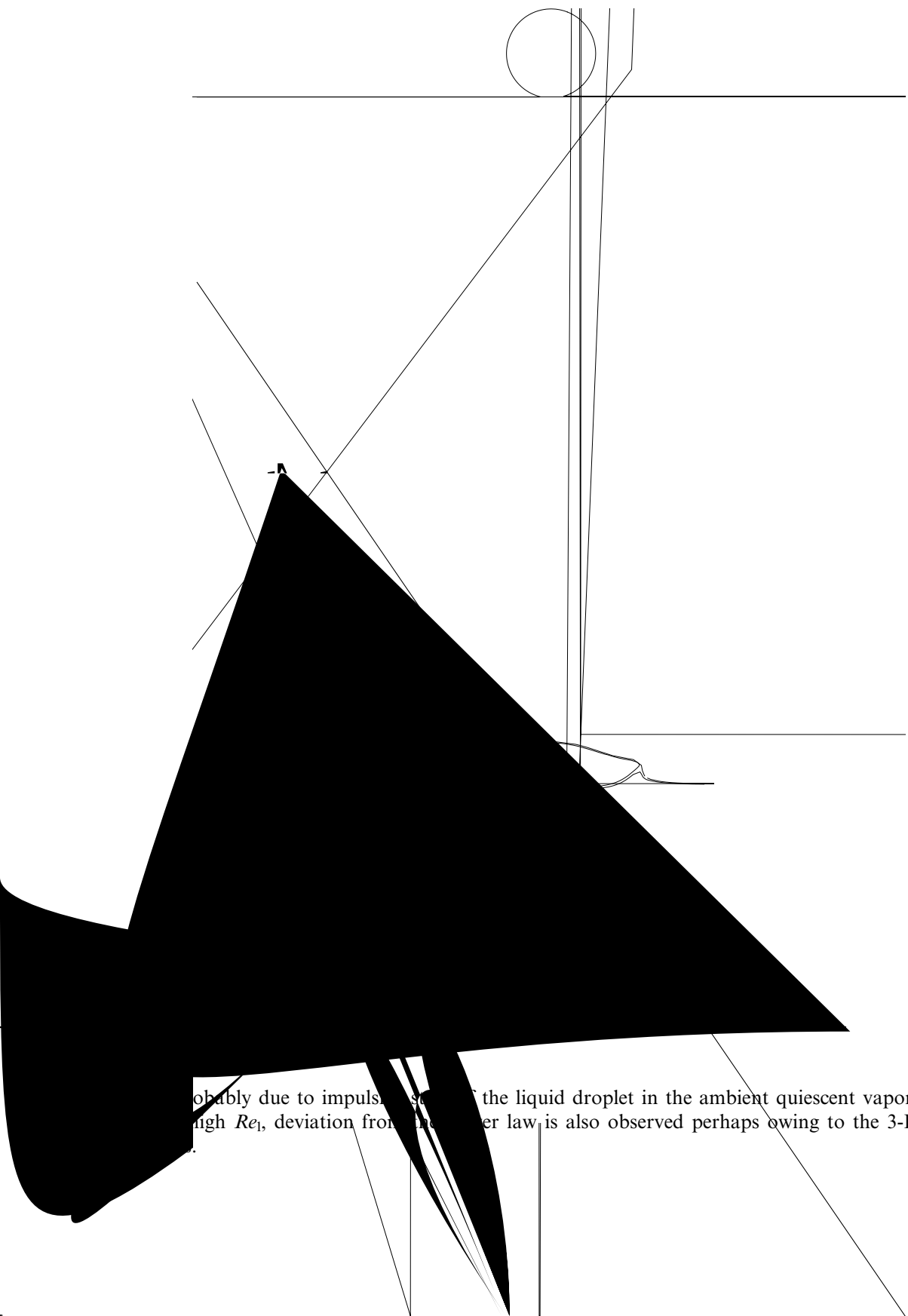
obably due to impulsive start of the liquid droplet in the ambient quiescent vapor. At longer high Re_l, deviation from the power law is also observed perhaps owing to the 3-D nature of

(a) Interface shapes

(b) Velocity vector at Ut/2R=0.5
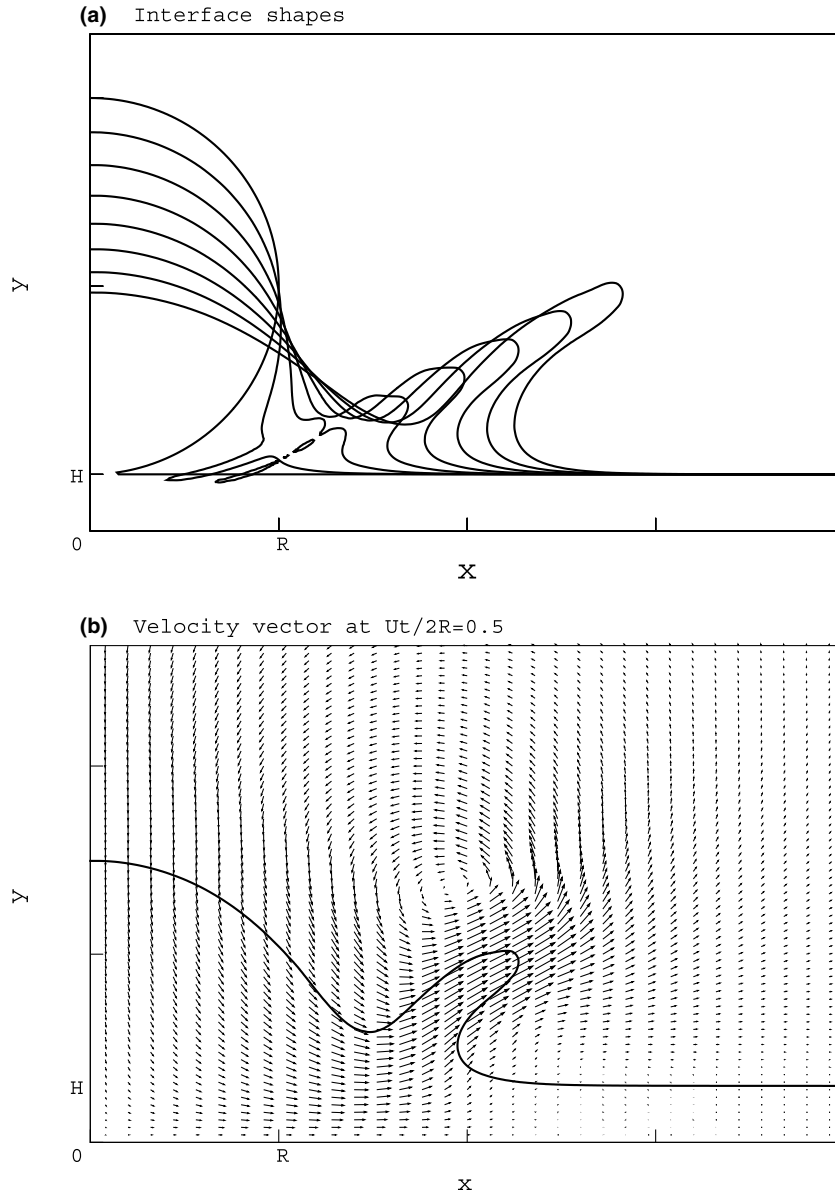
Fig. 18. (a) Interface shapes near the neck of the impact at $Re = 500$ with the interval of $Ut/2R = 0.1$ between $Ut/2R = 0.0$ and $Ut/2R = 0.7$, (b) instantaneous velocity vector field at $Ut/2R = 0.5$.

5. Concluding remarks

This paper is concerned with stabilizing the two-phase LBE formulation at high density and viscosity ratios. Most of previous LBE simulations have been carried out for fluids whose density ratio is less than 10 due to instability at high-density ratio. Therefore, the applicability of the LBE method has been very limited to some idealized situations. The density ratio (and the viscosity ratio) is greatly increased (e.g.,
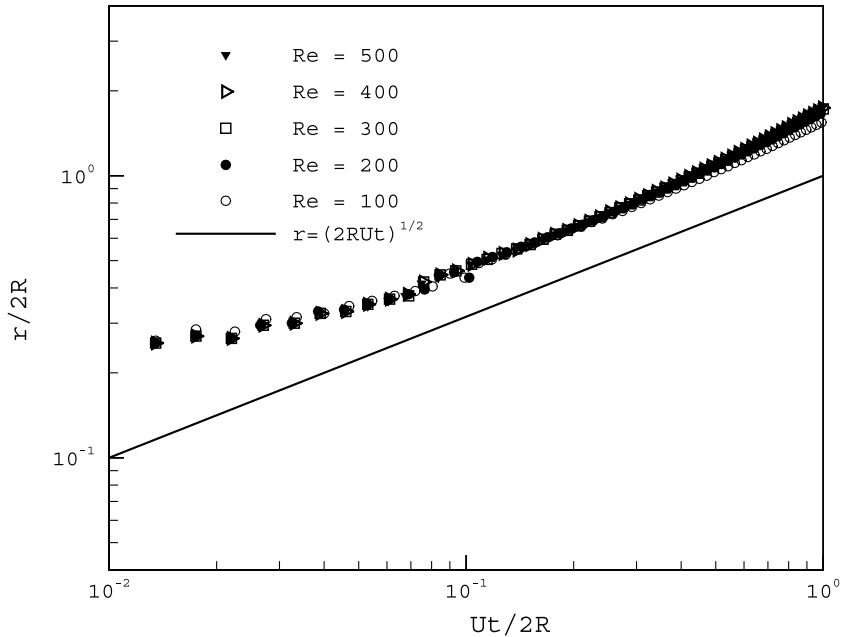
Fig. 19. Log–log plot of the spread factor $r/2R$ as a function of non-dimensional time $Ut/2R$. The straight line corresponds to the power law $r = \sqrt{2RUt}$.

>1000) by incorporating a collection of consistent discretization strategies. It comprises the low *Mach* number approximation, the stress and potential forms of the surface tension force, the incompressible transformation, and the consistent discretization of the intermolecular forcing terms.

A basic premise behind any LBE methods is that the Mach number of flows must be kept small, on which the present low Mach number approximation is based. The incompressibility of the fluids further removes potential numerical oscillations arising from the compressibility effect across the phase interface. The stress form of the surface tension force eliminates sub-grid level pressure oscillation due to the limited number of grid points in the phase interface region. By introducing chemical potential, it is possible to control interface thickness and surface tension at equilibrium. The discretization of the forcing term is of utmost importance in stabilizing the liquid–vapor LBE method. In particular, the forcing terms in the pre-streaming collision step and the post-streaming collision step must be treated differently. Otherwise, the solution becomes either unstable or overly diffusive.

The present LBE method has been validated over a series of benchmarks problems such as 1-D advection equation with a source term, and stationary and oscillatory droplets, and droplet splashing. The results are in excellent agreement with the previous analytic results. The ability of the present LBE method to accurately simulate the liquid–vapor flows at high density ratio holds a promise to expand applicability of the LBE method to practical CFD problems.

Acknowledgements

Appendix A

- D2Q9 model

  In the case of 2D 9-velocity model, the first derivative Eq. (64) can be recast in terms of grid indices.

$$\frac{\partial \phi}{\partial x}\bigg|_{(i,j)} = \Big[\phi_{(i+1,j)} - \phi_{(i-1,j)}\Big]\Big/3 + \Big[\phi_{(i+1,j+1)} - \phi_{(i-1,j-1)}\Big]\Big/12 + \Big[\phi_{(i+1,j-1)} - \phi_{(i-1,j+1)}\Big]\Big/12 \tag{A.1}$$

and

$$\frac{\partial \phi}{\partial y}\bigg|_{(i,j)} = \Big[\phi_{(i,j+1)} - \phi_{(i,j-1)}\Big]\Big/3 + \Big[\phi_{(i+1,j+1)} - \phi_{(i-1,j-1)}\Big]\Big/12 + \Big[\phi_{(i-1,j+1)} - \phi_{(i+1,j-1)}\Big]\Big/12, \tag{A.2}$$

in which i and j are grid indices in the x- and y-direction, respectively.

The second derivative Eq. (65) is calculated using the following finite difference scheme

$$\frac{\partial^2 \phi}{\partial x_k^2}\bigg|_{(i,j)} = [\phi_{(i+1,j+1)} + \phi_{(i-1,j+1)} + \phi_{(i+1,j-1)} + \phi_{(i-1,j-1)} + 4\phi_{(i+1,j)} + 4\phi_{(i-1,j)}$$
$$+ 4\phi_{(i,j+1)} + 4\phi_{(i,j-1)} - 20\phi_{(i,j)}]\Big/6. \tag{A.3}$$

- D3Q19 model

  In the case of 3D 19-velocity model, the first derivative Eq. (64) can be recast in terms of grid indices.

$$\frac{\partial \phi}{\partial x}\bigg|_{(i,j,k)} = \Big[\phi_{(i+1,j,k)} - \phi_{(i-1,j,k)}\Big]\Big/6 + \Big[\phi_{(i+1,j+1,k)} - \phi_{(i-1,j-1,k)}\Big]\Big/12$$
$$+ \Big[\phi_{(i+1,j-1,k)} - \phi_{(i-1,j+1,k)}\Big]\Big/12 + \Big[\phi_{(i+1,j,k+1)} - \phi_{(i-1,j,k-1)}\Big]\Big/12$$
$$+ \Big[\phi_{(i+1,j,k-1)} - \phi_{(i-1,j,k+1)}\Big]\Big/12, \tag{A.4}$$

$$\frac{\partial \phi}{\partial y}\bigg|_{(i,j,k)} = \Big[\phi_{(i,j+1,k)} - \phi_{(i,j-1,k)}\Big]\Big/6 + \Big[\phi_{(i+1,j+1,k)} - \phi_{(i-1,j-1,k)}\Big]\Big/12$$
$$+ \Big[\phi_{(i-1,j+1,k)} - \phi_{(i+1,j-1,k)}\Big]\Big/12 + \Big[\phi_{(i,j+1,k+1)} - \phi_{(i,j-1,k-1)}\Big]\Big/12$$
$$+ \Big[\phi_{(i,j+1,k-1)} - \phi_{(i,j-1,k+1)}\Big]\Big/12, \tag{A.5}$$

and

$$\frac{\partial \phi}{\partial y}\bigg|_{(i,j,k)} = \Big[\phi_{(i,j,k+1)} - \phi_{(i,j,k-1)}\Big]\Big/6 + \Big[\phi_{(i+1,j+1,k)} - \phi_{(i-1,j-1,k)}\Big]\Big/12 + \Big[\phi_{(i-1,j-1,k)} - \phi_{(i+1,j+1,k)}\Big]\Big/12$$
$$+ \Big[\phi_{(i,j+1,k+1)} - \phi_{(i,j-1,k-1)}\Big]\Big/12 + \Big[\phi_{(i,j-1,k+1)} - \phi_{(i,j+1,k+1)}\Big]\Big/12, \tag{A.6}$$

in which i, j, and k are grid indices in the x-, y-, and z-direction, respectively.

The second derivative Eq. (65) is calculated using the following finite difference scheme

$$\frac{\partial^2 \phi}{\partial x_k^2}\bigg|_{(i,j,k)} = [\phi_{(i+1,j+1,k)} + \phi_{(i-1,j-1,k)} + \phi_{(i+1,j-1,k)} + \phi_{(i-1,j+1,k)} + \phi_{(i+1,j,k+1)} + \phi_{(i-1,j,k-1)} + \phi_{(i+1,j,k-1)}$$
$$+ \phi_{(i-1,j,k+1)} + \phi_{(i,j+1,k+1)} + \phi_{(i,j-1,k-1)} + \phi_{(i,j+1,k-1)} + \phi_{(i,j-1,k+1)} + 2\phi_{(i+1,j,k)} + 2\phi_{(i-1,j,k)}$$
$$+ 2\phi_{(i,j+1,k)} + 2\phi_{(i,j-1,k)} + 2\phi_{(i,j,k+1)} + 2\phi_{(i,j,k-1)} - 24\phi_{(i,j)}]\Big/6. \tag{A.7}$$

References

[1] L.M. Pismen, Nonlocal diffuse interface theory of thin films and the moving contact line, Phys. Rev. E, 64, 2001, 021693-1.

[2] S. Chen, G.D. Doolen, Lattice Boltzmann method for fluid flows, Annu. Rev. Fluid Mech. 30 (1998) 329.

[3] A.K. Gunstensen, D.H. Rothman, S. Zaleski, G. Zanetti, A discrete Boltzmann equation model for non-ideal gases, Phys. Rev. A 43 (1991) 4320.

[4] X. Shan, H. Chen, Lattice Boltzmann model for simulating flows with multiple phases and components, Phys. Rev. E 47 (1993) 1815.

[5] X. Shan, H. Chen, Simulation of nonideal gases and liquid–gas phase-transition by the lattice Boltzmann-equation, Phys. Rev. E 49 (1994) 2941.

[6] M.R. Swift, W.R. Osborn, J.M. Yeomans, Lattice Boltzmann simulation of nonideal fluids, Phys. Rev. Lett. 75 (1995) 830.

[7] M.R. Swift, E. Orlandini, W.R. Osborn, J.M. Yeomans, Lattice Boltzmann simulations of liquid–gas and binary fluid systems, Phys. Rev. E 54 (1996) 5041.

[8] N.S. Martys, H. Chen, Simulation of multicomponent fluids in complex three-dimensional geometries by the lattice Boltzmann method, Phys. Rev. E 53 (1996) 743.

[9] X. He, S. Chen, R. Zhang, A lattice Boltzmann scheme for incompressible multiphase flow and its application in simulation of Rayleigh–Taylor instability, J. Comput. Phys. 152 (1999) 642.

[10] X. He, R. Zhang, S. Chen, G.D. Doolen, On the three-dimensional Rayleigh–Taylor instability, Phys. Fluids 11 (1999) 1143.

[11] R. Zhang, X. He, S. Chen, Interface and surface tension in incompressible lattice Boltzmann multiphase model, Comput. Phys. Commun. 129 (2000) 121.

[12] R. Zhang, X. He, G. Doolen, S. Chen, Surface tension effects on two-dimensional two-phase Kelvin–Helmholtz instabilities, Adv. Water Resour. 24 (2001) 461.

[13] X. Nie, G.D. Doolen, S. Chen, Lattice–Boltzmann simulations of fluid flows in MEMS, J. Stat. Phys. 107 (2002) 279.

[14] C.Y. Lim, C. Shu, X.D. Niu, Y.T. Chew, Application of lattice Boltzmann method to simulate microchannel flows, Phys. Fluids 14 (2002) 2299.

[15] S. Succi, Mesoscopic modeling of slip motion at fluid-solid interfaces with heterogeneous catalysis, Phys. Rev. Lett. 89 (2003) 064502.

[16] T. Lee, C.-L. Lin, Rarefaction and compressibility effects of the lattice Boltzmann equation method in a gas microchannel, in review, 2004.

[17] D.M. Anderson, G.B. McFadden, A.A. Wheeler, Diffuse-interface methods in fluid mechanics, Annu. Rev. Fluid Mech. 30 (1998) 139.

[18] D. Jamet, O. Lebaigue, N. Coutris, J.M. Delhaye, The second gradient method for the direct numerical simulation of liquid–vapor flows with phase change, J. Comput. Phys. 169 (2001) 624.

[19] T. Lee, C.-L. Lin, A pressure evolution lattice Boltzmann equation method for two-phase flow with phase change, Phys. Rev. E 67 (2003) 056703.

[20] X. He, X. Shan, G.D. Doolen, A discrete Boltzmann equation model for non-ideal gases, Phys. Rev. E 57 (1998) R13.

[21] X. He, L. Luo, A discrete Boltzmann equation model for non-ideal gases, Phys. Rev. E 55 (1997) R6333.

[22] D.J. Holdych, D. Rovas, J.G. Georgiadis, R.O. Buckius, An improved hydrodynamics formulation for multiphase flow lattice-Boltzmann models, Int.J. Mod. Phys. C 9 (1998) 1393.

[23] R.R. Nourgaliev, T.N. Dinh, T.G. Theofanous, D. Joseph, The lattice Boltzmann equation method: theoretical interpretation, numerics and implications, Int. J. Multiphase Flow 29 (2003) 117.

[24] A. Majda, J. Sethian, The derivation and numerical solution of the equations for zero Mach number combustion, Combust. Sci. Technol. 42 (1985) 185.

[25] M.S. Day, J.B. Bell, Numerical simulation of laminar reacting flows with complex chemistry, Combust. Theory Modelling 4 (4) (2000) 535.

[26] Y. Chen, S.L. Teng, S. Shukuwa, H. Ohashi, Lattice Boltzmann simulation of two-phase fluid flows, Int. J. Mod. Phys. C 9 (1998) 1383.

[27] C. HirschNumerical Computation of Internal and External Flows, vol. II, John Wiley and Sons, New York, 1990.

[28] T. Lee, C.-L. Lin, An Eulerian description of the streaming process in the lattice Boltzmann equation, J. Comput. Phys. 185 (2003) 445.

[29] T. Inamuro, T. Ogata, F. Ogino, Lattice Boltzmann Simulation of Bubble Flows, Computational Science-ICCS2003 LNCS 2657, Springer-Verlag, Berlin, 2003, 1015.

[30] T. Inamuro, T. Ogata, S. Tajima, N. Konishi, A lattice Boltzmann method for incompressible two-phase flows with large density differences, J. Comput. Phys. 198 (2004) 628.

[31] K. Sankaranarayanan, X. Shan, I.G. Kevrekidis, S. Sundaresan, Analysis of drag and virtual mass forces in bubbly suspensions using an implicit formulation of the lattice Boltzmann method, J. Fluid Mech. 452 (2002) 61.

[32] Y.-H. Qian, S.-Y. Chen, Dissipative and dispersive behavior of lattice-based models for hydrodynamics, Phys. Rev. E 61 (2000) 2712.

[33] B.T. Nadiga, S. Zaleski, Investigations of a two-phase fluid model, Euro. J. Mech. B: Fluids 15 (1996) 885.

[34] D.-Y. Hsieh, X.-P. Wang, Phase transition in van der Waals fluid, SIAM J. Appl. Math. 57 (4) (1997) 871.

[35] D. Jacgmin, An energy approach to the continuum surface method, in: 34th Aerospace Sciences Meeting, Reno, NV 96, 1996, p. 0858.

[36] O. Filippova, D. Hänel, A novel lattice BGK approach for low Mach number combustion, J. Comput. Phys. 158 (2000) 139.

[37] J.S. Rowlinson, B. Widom, Molecular Theory of Capillary, Oxford Press, Oxford, 1989.

[38] J. Lowengrub, L. Truskinovsky, Quasi-incompressible Cahn–Hilliard fluids and topological transitions, Proc.R. Soc. Lond. A 454 (1998) 2617.

[39] A.D. Angelopoulos, V.N. Paunov, V.N. Burganos, A.C. Payatakes, Lattice Boltzmann simulation of nonideal vapor–liquid flow in porous media, Phys. Rev. E 57 (3) (1998) 3237.

[40] L. Luo, Theory of the lattice Boltzmann method: Lattice Boltzmann models for nonideal gases, Phys. Rev. E 62 (2000) 4982.

[41] B.J. Palmer, D.R. Rector, Lattice-Boltzmann algorithm for simulating thermal two-phase flow, Phys. Rev. E 61 (2000) 5295.

[42] T. Lee, C.-L. Lin, A characteristic Galerkin method for discrete Boltzmann equation, J. Comput. Phys. 171 (2001) 336.

[43] M. Dai, J.B. Perot, D.P. Schmidt, Heat transfer within deforming droplets, in: Proceedings of ASME, Internal Combustion Engine Division, September, New Orleans, 2002.

[44] H. Lamb, Hydrodynamics, Dover, New York, 1932.

[45] C. Josserand, S. Zaleski, Droplet splashing on a thin liquid film, Phys. Fluids 15 (2003) 1650.

[46] D.A. Weiss, A.L. Yarin, Single drop impact ont liquid films: Neck distortion, jetting, tiny bubble entrainment, and crown formation, J. Fluid Mech. 385 (1999) 229.

[47] H.-Y. Kim, Z. Feng, J.-H. Chun, Instability of a liquid jet emerging from a droplet upon collision with a solid surface, Phys. Fluids 12 (2000) 531.